AMERICAN UNIVERSITY OF BEIRUT

MAGNETIZATION DYNAMICS OF CoFe THIN FILMS GROWN BY PULSED LASER DEPOSITION

by

KHALIL IBRAHIM EL ACHI

A thesis
submitted in partial fulfillment of the requirements
for the degree of Master of Science
to the Department of Physics
of the Faculty of Arts and Sciences
at the American University of Beirut

Beirut, Lebanon
January 2024

AMERICAN UNIVERSITY OF BEIRUT

MAGNETIZATION DYNAMICS OF CoFe THIN FILMS GROWN BY PULSED LASER DEPOSITION

by

KHALIL IBRAHIM EL ACHI

Approved by:

Mhaidar

Dr. Mohammad Haidar, Assistant Professor — Advisor

Physics

Dr. Samih Isber, Professor — Member of Committee

Physics

Dr. Michel Kazan, Professor — Member of Committee

Physics

Date of thesis defense: January 17, 2024

AMERICAN UNIVERSITY OF BEIRUT

THESIS RELEASE FORM

Student Name: El Achi Khalil Ibrahim
Last First Middle

I authorize the American University of Beirut, to: (a) reproduce hard or electronic copies of my thesis; (b) include such copies in the archives and digital repositories of the University; and (c) make freely available such copies to third parties for research or educational purposes

[✓ **As of the date of submission of my thesis**]

___ **After 1 year from the date of submission of my thesis .**

___ **After 2 years from the date of submission of my thesis .**

___ **After 3 years from the date of submission of my thesis .**

18/01/2024
Signature Date

ACKNOWLEDGEMENTS

I would like to take the opportunity to acknowledge that this whole work was done in the spawn of the Fall semester in the American University of Beirut's Physics department. From the deposition, testing, measurement, and analysis. The process was long and arduous but it was done successfully and fruitfully.

First and foremost, sincere gratitude should be expressed to my advisor and mentor during this whole period Dr. Mohammad Haidar who closely monitored my progress, assisted with the data-taking and deposition process, trained me on the vast equipment used, and personally aided in administrative and academic endeavors during my time as a masters student. His expertise, insightful feedback, and commitment to academic excellence have been paramount of shaping the development of this thesis.

I am thankful to the members of my thesis committee, Dr. Samih Isber and Dr. Michel Kazan, for their time and knowledge in providing constructive feedback and valuable suggestions that have significantly strengthened the quality of this work.

Moreover, I extend my appreciation to all those individuals who may not be explicitly mentioned here but have, in various ways, contributed to the successful completion of this thesis. Your assistance, whether big or small, has not gone unnoticed.

My heartfelt thanks go to my family and friends for their unwavering support, understanding, and encouragement throughout this academic journey. Their belief in my abilities and their motivation has been a constant source of inspiration.

Finally and most honorably, extreme gratitude and thanks go to the team of Engineers and Lab Supervisors in the Kamal A. Shair Central Research Science Laboratory (CRSL) for their assistance, training, help, and responsiveness. I am very thankful for everyone on the team who provided their expertise and prowess which aided and quite frankly accelerated the experimental procedure of culturing the films.

Thank you to everyone who has played a role in this academic achievement. Your support has been indispensable, and I am truly grateful for the collaborative effort that has brought this thesis to fruition.

ABSTRACT
OF THE THESIS OF

Khalil El Achi for Master of Science
Major: Physics

Title: Magnetization Dynamics of CoFe Thin Films Grown by Pulsed Laser Deposition

Magnetic damping plays a pivotal role in devices harnessing the electronic spin degree of freedom, significantly influencing their energy efficiency and operational speed. Despite its crucial role, the persistently high Gilbert damping in common ferromagnetic materials, typically on the order of 10^{-3}, presents a challenge for applications in spintronics and spin-orbitronics that require materials with ultra-low damping characteristics. Alternative materials, such as Heusler alloys and magnetic insulators, have showcased significantly lower damping coefficients below 10^{-4}, primarily due to the absence of conduction electrons. Unfortunately, despite their low damping attributes, these materials pose growth challenges and are incompatible with the widely used Complementary Metal-Oxide-Semiconductor (CMOS) technology, limiting their practical utility. Recent developments in material science search for low-damping material, introduce promising prospects. Cobalt and iron binary alloys, particularly $Co_{20}Fe_{80}$, challenge the conventional limitations by exhibiting relatively low damping coefficients. Theoretical predictions by Mankovsky et al. propose a damping coefficient of 5×10^{-4} in $Co_{20}Fe_{80}$, highlighting a unique band structure with a sharp minimum in the density of states at the Fermi level. This minimum aligns with the alloy concentration where the least magnetic damping occurs. Subsequent experimental studies by Schoen et al. validate these theoretical predictions, underscoring the potential of $Co_{20}Fe_{80}$ alloys as materials with minimal damping characteristics. The focus of this thesis is to study the magnetization dynamics of $Co_{60}Fe_{40}$ thin films prepared through Pulsed Laser Deposition (PLD). The overarching goal is to develop high-quality nanometer-thick films. The investigation kicks off by scrutinizing the characteristics of CoFe films under diverse deposition parameters, manipulating laser energy and temperature to discern optimal conditions. Once these optimal parameters are identified, a systematic exploration of thickness dependence follows, encompassing variations in the CoFe layer thickness within the range of 10 to 25 nm. Moreover, the study extends to exploring the spin-pumping effect in bilayers of CoFe/Pt. In this aspect, the thickness of the Pt layer is systematically varied, enabling the calculation of the spin diffusion length in Pt. This meticulous and systematic study aims to yield valuable insights applicable to the realms of magnonics, spintronics, and spin Hall devices.

Keywords: CoFe thin films, Ferromagnetic Resonance, Lock-In Technique, Pulsed Laser Deposition, Gilbert Damping Factor, Saturation Magnetization, Spin-Pumping, and Spin Mixing Conductance.

TABLE OF CONTENTS

ILLUSTRATIONS

TABLES

ABBREVIATIONS AND SYMBOLS

FCC	Face-Centered Cubic
BCC	Body-Centered Cubic
PLD	Pulsed Laser Deposition
FM	Ferromagnetic
FMR	Ferromagnetic Resonance
LLG	Landau-Lifshitz-Gilbert
SEM	Scanning Electron Microscopy
EDX	Energy Dispersive X-ray
IP	In-Plane
OOP	Out-of-plane
MCA	Magnetocrystalline Anisotropy
RF	Radio Frequency
CPW	Coplanar Waveguide
CoFe	Cobalt Iron Alloy
α_G	Gilbert Damping Coefficient
M_S	Saturation Magnetization
M	Magnetic Moment
γ	Gyromagnetic Ratio
Pt	Platinum
FWHM	Full Width at Half Maximum
μ_B	Bohr Magneton
g	Spectroscopic Factor
$g^{\uparrow\downarrow}$	Spin Mixing Conductance
λ_{SD}	Spin Diffusion Coefficient

Chapter 1

Introduction

1.1 Introduction to Magnetization

The first chapter will discuss fundamental concepts in magnetism. First, a general basis of the characteristics of magnetic materials will be discussed, with a special focus on ferromagnetic materials. Second, we will describe the magnetization dynamics in thin films, which are governed by the Landau-Lifshitz equation of motion. Then, we will discuss magnetization relaxation using the Gilbert formalism. Finally, we will explain the spin-pumping phenomenon, which is a new concept in spintronics that affects magnetic relaxation.

1.1.1 *Magnetic Moment*

Magnetic materials have been known for a long time, dating back to the early days of Greece, during which these materials were implemented in the technology for finding directions. However, magnetism can only be explained based on the foundation of quantum mechanics, where an electron can have two different magnetic states: either spin up or spin down. The magnetism of materials is associated with a small current-carrying loop known as magnetic moments as shown in figure 1.2. For example, the magnetic moment of an electron orbiting around the nucleus is defined as:

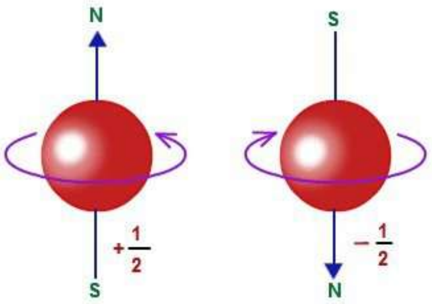

Figure 1.1: Schematic representation of the electron magnetic spin

$$d\vec{m} = IdS \tag{1.1}$$

Here, I is the current carrying loop, and dS is the normal vector. By definition, the magnetic moment is a vector quantity. In materials, magnetic moments are added vectorially, where the net sum is zero for normal materials or a non-zero value for magnetic materials. Magnetic moments can interact with an external magnetic field or with another magnetic moment, as explained below. However, a microscope quantity referred to as magnetization (M) is commonly used and defined as the sum of the magnetic moment per unit volume (V)

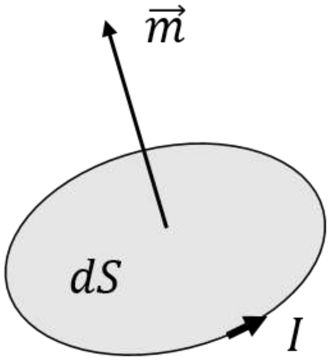

Figure 1.2: Elementary magnetic moment $\vec{m}$

$$M = \sum \frac{m}{V} \tag{1.2}$$

Einstein de Haas experiment proves that the magnetic moment (m) is related to the angular momentum (L) through a fundamental constant the gyromagnetic ratio (γ) [1] where

$$m = \gamma L \tag{1.3}$$

1.1.2 *Interaction of Magnetic Moment with an External Magnetic Field*

When a magnetic moment is placed in a magnetic field, it will rotate to align with the direction of the magnetic field vector, as illustrated in Figure 1.3. This rotation leads to a change in its energy, given by:

$$E = -\vec{m} \cdot \vec{B} = -mB\cos(\theta) \tag{1.4}$$

Here, θ is the angle between the magnetic moment and the applied field. It is minimum when θ is 90° and maximum when θ is 180°.

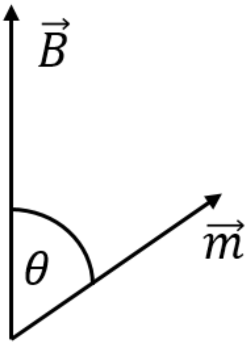

Figure 1.3: Precession of a magnetic moment $\vec{m}$ in a magnetic field B

1.1.3 *Types of Magnetic Materials*

1.1.3.1 Diamagnetism

When a diamagnetic material is exposed to an external magnetic field, it weakly resists the field and aligns its magnetic moment in the opposite direction to the field. Diamagnetic materials do not exhibit magnetic properties due to the absence of unpaired electrons. Elements that exhibit diamagnetic behavior include metals and non-metals such as salts (NaCl, CaCl, ...), ions (Li^{+}, Ca^{2+}, ...), and noble gases (He, Ar, ...), as well as superconductors, which are ideal diamagnetic materials.

1.1.3.2 Paramagnetism

Paramagnetic materials constitute another class of materials that exhibit a positive response to an applied magnetic field. These neutral materials can develop an induced magnetic moment when subjected to an external magnetic field, a phenomenon originating from the presence of unpaired electrons. The induced magnetization (M) is proportional to the strength of the applied field, expressed as $M = \chi H$, where χ is the susceptibility constant. For paramagnetic materials, χ is positive. Once the external magnetic field is turned off, the material loses its induced magnetization and returns to its initial state. It is worth noting that the majority of elements in the periodic table are paramagnetic, such as Cu, Pt, and others.

1.1.3.3 Ferromagnetism

Ferromagnets are a select group of elements, such as Fe, Co, Ni, and their alloys, that possess inherent magnetism. These materials exhibit a net spontaneous magnetization due to the presence of unpaired electrons, even in the absence of an applied magnetic field. Within a ferromagnetic material, magnetic domains are formed where magnetic moments are initially arranged in a random orientation. When a magnetic field is applied, these materials respond positively, causing all magnetic moments to align parallel to the magnetic field, resulting in an ordered state. Even after the removal of the magnetic field, these materials retain their magnetic properties, as illustrated in Figure 1.4 [2]. Such materials find extensive applications in various technologies, ranging from permanent magnets to data storage and memory applications, as well as magnetic sensors [3].

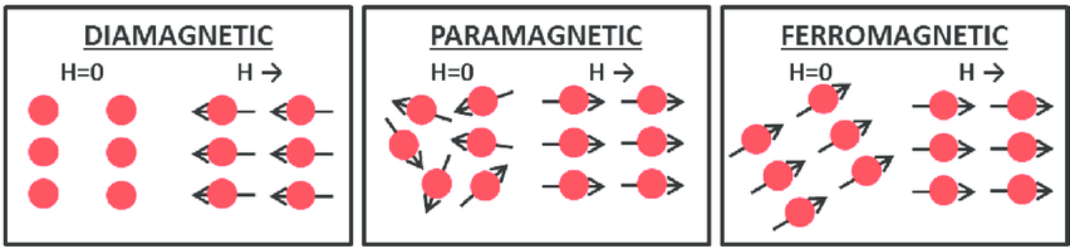

Figure 1.4: Behavior of the individual magnetic moments in the absence and presence of a magnetic field for a Diamagnetic, Paramagnetic, and Ferromagnetic material, taken from [4]

1.1.4 *Magnetic Hysteresis*

Ferromagnets have a unique property called hysteresis which means that the magnitude of the magnetization changes depending on how the magnetic field is applied. Figure 1.5 shows the trajectory of the magnetization by the application of magnetic fields. In the absence of any magnetic field, the magnetization, that is the net magnetic moment in the sample is valued around the remnant magnetization $\pm M_r$. As one applies a magnetic field it drives the magnetic moment to positive or negative saturation $\pm M_s$.

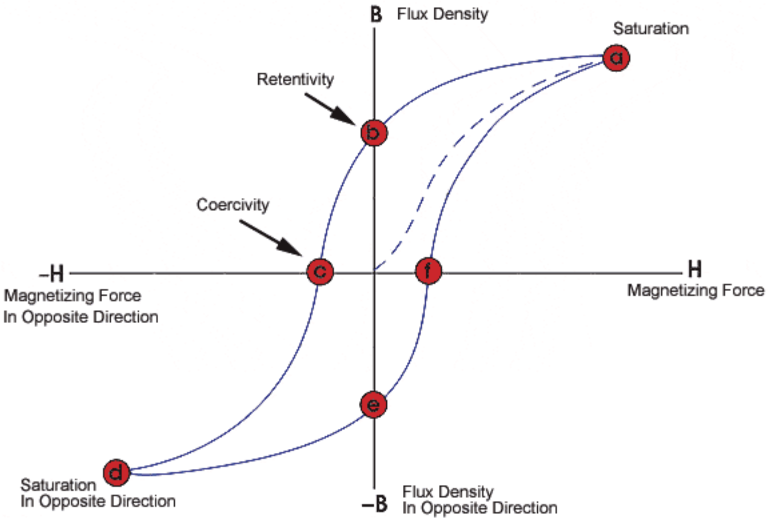

Figure 1.5: Magnetic Hysteresis Loop showing the variation of the Magnetic Flux Density B as a function of the Magnetic Field H

The effect of the magnetic field can be visualized through Figure 1.6. Once all the magnetic moments become parallel to the applied magnetic field, the magnetization of the material will be maximized achieving the saturation.

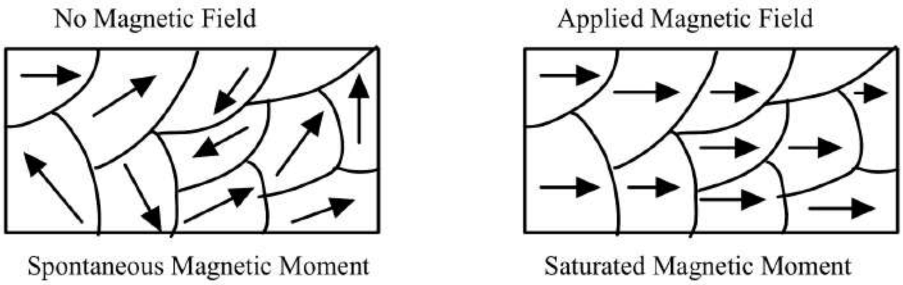

Figure 1.6: Representation of the magnetic moments in a Ferromagnet in the absence and presence of a Magnetic Field

1.2 Magnetic Interaction

Now, let us discuss the interaction between adjacent magnetic moments.

1.2.1 ***Magnetic Dipolar Field***

Consider two magnetic dipoles m_1 and m_2 separated by a distance r, these dipoles will interact with each other where the energy formed between them is described by

$$E = \frac{\mu_0}{4\pi r^3}\left[m_1.m_2 - \frac{3}{r^2}(m_1.r)(m_2.r)\right] \tag{1.5}$$

The magnetic dipolar energy is proportional to the degree of alignment of the magnetic moments and their perspective separation. This interaction is described as a long-range interaction.

1.2.2 ***Exchange Interaction***

Two adjacent magnetic moments can interact with each other over a short length. This interaction is known as exchange interaction. The exchange interaction is responsible for the alignment of magnetic order in ferromagnets. It originated from the Pauli exclusion principle, stating that two electrons with the same spin cannot occupy the same quantum state simultaneously. The exchange energy ($E_{exchange}$) can be described using the Heisenberg model, which is commonly expressed as:

$$E_{excahnge} = -J\sum_{i,j} S_i S_j \tag{1.6}$$

Where J is the exchange constant eluding to the magnitude of the interaction, and S_i & S_j are the perspective spin vectors of the magnetic moments. For a positive J

the exchange energy is minimized when neighboring spins are aligned parallel to each other i.e. forming a ferromagnetic state. However, for a negative J the exchange energy is minimized when neighboring spins are aligned antiparallel to each other i.e. forming an antiferromagnetic state.

1.2.3 *Magnetic Anisotropy in Ferromagnets*

Anisotropy refers to the reliance of a material or object's characteristics on the angles formed between the applied field directions and certain preferred orientations. These orientations may be dictated by the material's structure, the shape of the object, or (when considering properties in alternating current fields) the orientations of specific external constant fields.

Two anisotropic dependence emerge in these materials:

- Shape Anisotropy: This type of anisotropy is associated with the shape of a magnetic object. For example, a long, thin magnetic particle will have different magnetic properties along its length compared to its width.
- Crystalline Anisotropy: This is related to the crystal structure of a material. In crystalline materials, the arrangement of atoms and the symmetry of the crystal lattice can affect the preferred direction of magnetization. Different crystallographic directions may have different magnetic properties [5].

1.3 Magnetization Dynamics in magnetic thin films

1.3.1 *Landau-Lifshitz Equation of Motion*

When a magnetic film is placed in a magnetic field, the static magnetization follows an equilibrium direction. The magnetization can be derived out-of-equilibrium by external sources such as light or radio-frequency waves. These excitations can emit microwave oscillations with frequencies ranging from a few Megahertz (MHz) to hundreds of Gigahertz (GHz) with a time scale that spans nanosecond to picosecond. The magnetization dynamics is described by the Landau-Lifshitz [6], where the evolution of the magnetization with time is represented by

$$\frac{\partial M}{\partial t} = -\gamma M \times H_{eff} \tag{1.7}$$

Where γ is the gyromagnetic ratio and H_{eff} is the effective field which is the sum of all magnetic fields: the dipolar, the exchange, and the anisotropy fields,

$$H_{eff} = -\frac{\delta U}{\delta M} \tag{1.8}$$

By solving this differential equation one can find the eigenstates and the eigenvalues of the oscillations. One can obtain the dispersion relation of the magnetic excitations while considering the effective field and its relative orientation to the magnetization. Below we will derive the dispersion relation for two cases while the external magnetic field is applied in-plane and out-of-plane. In this thesis, our magnetic films have no anisotropy and we neglect the exchange interaction as we did not observe a higher order of the oscillations. Hence the effective magnetic field is dominated by the external field mainly.

1.3.2 *Solution of the LLG Equation*

To start by solving the LLG equation let's consider a ferromagnet in the presence of an internal ac magnetic field with an oscillating magnetization as explained in Gurevich et al. [7].

Then when factoring both the constant and alternating components of the magnetic field and the magnetization the following can be written:

$$H = H_0 + \bar{h} \tag{1.9}$$

$$M = M_0 + \bar{m} \tag{1.10}$$

When only factoring in the constant terms and omitting the alternating contribution, plugging the magnetic field and magnetization into eq. 1.7 one gets:

$$M_0 \times H_0 = 0 \tag{1.11}$$

This represents that the magnetization and Magnetic field vectors are parallels which is the equilibrium direction of the magnetization.

When reconsidering the ac contribution and taking 1.11 consideration, the linearized equation of motion becomes:

$$\frac{\partial \bar{m}}{\partial t} + \gamma \bar{m} \times H_0 = -\gamma M_0 \times \bar{h} \tag{1.12}$$

To solve the above equation, consider the ac contribution of the magnetic field $\bar{h}$

and magnetization $\bar{m}$ are sinusoidal time-dependent:

$$\dot{h} = he^{i\omega t} \tag{1.13}$$

$$\dot{m} = me^{i\omega t} \tag{1.14}$$

$$\tag{1.15}$$

Plugging those back into 1.12, the linearized equation becomes:

$$i\omega m + \gamma m \times H_0 = -\gamma M_0 \times h \tag{1.16}$$

After undertaking the cross products and projecting the magnetization and magnetic field vectors into the perspective Cartesian coordinate system, a set of three equations is deduced:

$$i\omega m_x + \gamma H_0 m_y = \gamma M_0 h_y \tag{1.17}$$

$$-\gamma H_0 m_x + i\omega m_y = \gamma M_0 h_x \tag{1.18}$$

$$i\omega m_z = 0 \tag{1.19}$$

Solving the set of equations to get the components of the magnetization in terms of the magnetic field components as such:

$$m_x = \chi h_x + i\chi_a h_y \tag{1.20}$$

$$m_y = -i\chi_a h_y + \chi h_y \tag{1.21}$$

$$m_z = 0 \tag{1.22}$$

Where $\omega_H = \gamma H_0$, $\chi - \frac{\gamma M_0 \omega_H}{\omega_H^2 - \omega^2}$, and $\chi_a = \frac{\gamma M_0 \omega}{\omega_H^2 - \omega^2}$. The solution 1.20 can be written in tensor formalism:

$$m = \bar{\chi} h \tag{1.23}$$

Where $\bar{\chi}$ is the magnetic susceptibility and is written in the form of

$$\bar{\chi} = \begin{pmatrix} \chi & i\chi_a & 0 \\ -i\chi_a & \chi & 0 \\ 0 & 0 & 0 \end{pmatrix} \tag{1.24}$$

1.3.3 *Generalized Case of an Ellipsoid*

To understand the impact of an externally applied field, take a small ellipsoidal region which is a generic case to study, that can be used to describe more specific cases later on.

Without solving boundary condition, the relationship from magnetostatics can illustrate that the magnetic field is written by:

$$H = H_e + H_{dem} = H_e - \bar{N}M \tag{1.25}$$

Where H_e is the external magnetic field and H_{dem} is the demagnetization contribution which can be written in the form of the demagnetization tensor $H_{dem} = -\bar{N}M$.

The tensor $\bar{N}$ includes the demagnetization factors N_x, N_y, N_z which are the perspective axes of the ellipsoidal shape previously taken. With that, one can assume that $N_x + N_y + N_z = 4\pi$.

Then one can rewrite the constant and alternating contribution with the addition of the demagnetization terms:

$$H_0 = H_{e0} - \bar{N}M_0 \tag{1.26}$$

$$h_0 = h_{e0} - \bar{N}m_0 \tag{1.27}$$

Then we will use these correction factors back in the solution of the section 1.3.2. Recall the equilibrium condition in eq. 1.11, adding the correction term it then becomes:

$$M_0 \times (H_{e0} - \bar{N}M_0) = 0 \tag{1.28}$$

Then plugging the correction terms into the linearized solution in 1.12 it becomes:

$$i\omega m + \gamma m(H_{e0} - \bar{N}M_0) + \gamma(\bar{N}M_0) \times M_0 = 0 \tag{1.29}$$

To proceed with solving this equation, lay out the demagnetization tensor as

$$\bar{N} = \begin{pmatrix} N_{xx} & N_{xy} & N_{xz} \\ N_{xy} & N_{yy} & N_{yz} \\ N_{xz} & N_{xy} & N_{zz} \end{pmatrix} \tag{1.30}$$

One gets two linear equations:

$$(i\omega + \gamma N_{xy}M_0)m_x + \gamma(H_{e0z} - NzzM_0 + N_{yy}M_0)m_y = 0 \tag{1.31}$$

$$-\gamma(H_{e0z} - NzzM_0 + N_{xx}M_0)m_x + (i\omega + \gamma N_{xy}M_0)m_y = 0 \tag{1.32}$$

To ensure that these equations are set to be compatible, the condition for the frequency of the eigenoscillations is as such:

$$w_0^2 = (\omega_H + \gamma N_{xx}M_0)(\omega_H + \gamma N_{yy}M_0) - \gamma^2 N_{xy}^2 M_0^2 \tag{1.33}$$

Where as defined above $\omega_H = \gamma H_0 = \gamma(H_{e0} - \bar{N}M_0)$

The frequency that governs the maximum absorption of the electromagnetic energy is set to be the ferromagnetic resonance frequency. Simplifying the relationship of 1.33 by assuming that the external field is applied along one of the axes of the ellipsoid, reduces $\bar{N}$ to a diagonal matrix. Then the Kittel equation is obtained [8]. Which takes the following form:

$$w_0^2 = \gamma^2(H_{e0} + (N_x - N_z)M_0)(H_{e0} + (N_y - N_z)M_0) \tag{1.34}$$

Taking the condition that the sample is an infinitely long thin plate, the magnetization direction can be aligned either tangential to the film or normal to it.

Thus, in the case of In-Plane (IP) magnetization, either N_x or N_y would be equal to 4π and $N_z = 0$.

The Kittel equation for IP mode will then be written as:

$$\omega_0^2 = \gamma^2 H_{e0}(H_{e0} + 4\pi M_0) \tag{1.35}$$

In the case when the magnetization is perpendicular to the surface, or in Out-of-plane (OOP) mode, Both $N_x = N_y = 0$ and $N_z = 4\pi$. And the Kittel equation for OOP mode will then be written as:

$$\omega_0 = \gamma(H_{eo} - 4\pi M_0) \tag{1.36}$$

1.3.4 *Gilbert Damping Term*

The oscillations of magnetizations are accompanied by the dissipative of energy to other degrees of freedom in the system such as the phonons, magnons, and thermal energies. In this section, we will describe the dissipative term phenomenological as described by the Gilbert damping coefficient. An additional dissipative term should be added to LL equation to account for magnetic losses. The equation of motion is written as

$$\frac{\partial M}{\partial t} = -\gamma M \times H_{eff} - \frac{\gamma\lambda}{M^2} M \times (M \times H_{eff}) \tag{1.37}$$

where λ is the dissipation parameter with the same units of the magnetic field. In the previous equation the $M \times H_{eff}$ term can be replaced by $-\gamma\frac{\partial M}{\partial t}$ which allows us to introduce the Gilbert damping factor which is a dimensionless parameter: $\alpha_G = \frac{\lambda}{M}$. Therefore, the equation of motion is reduced to the Landaue-Lifshcitz-Gilbert (LLG) equation

$$\frac{\partial M}{\partial t} = -\gamma M \times H_{eff} + \frac{\alpha_G}{M} M \times (M\frac{\partial M}{\partial t}) \tag{1.38}$$

where the term to the left describes the evolution of the magnetization vector with time, the first term to the right hand describes the precessional motion of the magnetization and the second term to the right characterizes the damping term.

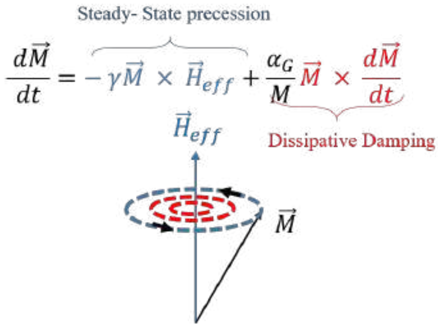

Figure 1.7: Representation of the LLG equation for the precession and damping of magnetic moment

1.3.4.1 Sources and Mechanism of Damping

The Gilbert damping characterizes the dissipation energy associated with the magnetization. It can be originated from several sources and active mechanisms in transition metals ferromagnets. Below we will briefly explain these mechanisms.

I- Magnon-electron collision: Berger has provided a simple picture of spin-wave relaxation in ferromagnetic metals [9]. In this conceptual framework, a magnon with energy $E(q) = \hbar\omega$ collides with an electron of energy $\epsilon_{k,s}$ where s denotes its spin. The magnon is annihilated during the collision, and the electron is transferred from one energy band to another with higher energy. Two cases could be distinguished. In the first case, the magnon-electron interaction conserves spin angular momentum (e.g., s-d exchange interaction), and the electron must flip its spin during the collision. In the second case, the interaction does not conserve spin momentum (e.g., spin-orbit coupling). The magnon relaxation time in both processes relies on the overlap between the spectral density of the occupied and unoccupied states around the Fermi level. The relaxation time exhibits a linear increase with frequency ω, with a constant factor.

II- Elliot-Yafet mechanism: magnon-phonon scattering In this scenario, magnetization relaxation occurs due to the interaction between a magnon and lattice vibrations. The process involves the destructive of spin precession by a phonon, assisted by a spin flip of the electron state. This interaction is facilitated by the spin-orbit interaction. In the presence of spin-orbit interaction, electron wavefunctions are a mix of spin-up and spin-down states, leading to finite spin-flip probabilities induced by phonon scattering.

III-Kambersky's torque model explains the intriguing relationship between temperature and damping in transition metals like Fe, Co, and Ni [10]. In this model, the damping of a uniform precession is shaped by both spin-orbit coupling and electron-lattice scattering. The process involves two steps: first, a uniform magnon transforms into an electron-hole pair due to spin-orbit coupling, and then this pair is scattered by lattice vibrations. In the Landau-Lifshitz formulation, the magnetization's magnitude remains constant, but its direction changes. The spin-orbit interaction causes the precession of magnetization to coincide with variations in the energy of electron states and transitions between these states.

1.3.4.2 Breathing Fermi Surface

The initial component of the effective field accounts for the change in spin-orbit energy concerning the magnetization's orientation. This element induces a modification in the Fermi surface [11]. Consequently, certain occupied states below the Fermi level are elevated above it, while other unoccupied states above the Fermi level are shifted downward. The resulting distribution of out-of-equilibrium electrons is restored to equilibrium through intraband transitions caused by scattering. This phenomenon is commonly referred to as a breathing Fermi surface [12]. In recent studies, various theoretical investigations have been conducted to calculate the Gilbert damping parameter for different 3d transition metallic ferromagnets, including Fe, Co, and Ni, as well as their respective alloys such as CoxFe$1-x$, CoxNi$1-x$, and NixFe$1-x$ using first-principle calculations [13], [14]. These calculations provide precise values of α by considering the impact of spin-orbit coupling and the breathing Fermi surface model. It is noteworthy that the transition of α across different concentrations of atoms in binary ferromagnetic alloys exhibits similar trends in both Mankovsky et al. and Turek et al.'s calculations.

1.3.5 *Spin Hall Effect and Spin Pumping*

Consider a charge current transverse a conductor in the longitudinal direction. When it is exposed to a magnetic field, oriented perpendicular to the film, a Lorentz force acting on the flow of the electron causes it to deflect along the transverse direction. This motion of charges causes an accumulation of positive and negative charges across the conductor resulting in an electric field along the transverse direction. This induced voltage is known as Hall voltage. A similar process could be observed in conductors with heavy metals known as the spin Hall effect (SHE), illustrated in figure 1.8. Consider a conductor with a strong spin-orbit coupling such as platinum, tungsten, or other spin Hall material. When a current passes through the conductor the spin-orbit coupling leads to a split of electrons according to their spins such that spin-up and spin-down electrons will be deflected along opposite surfaces. This imbalance of charges results in a voltage known as spin Hall voltage. While this process does not require an external magnetic field it is strongly observed in materials with a high atomic number of strong spin-orbit coupling. This process has been observed recently which represents an innovative method to create pure spin-polarized and found several applications in the field of spintronics and magnonics.

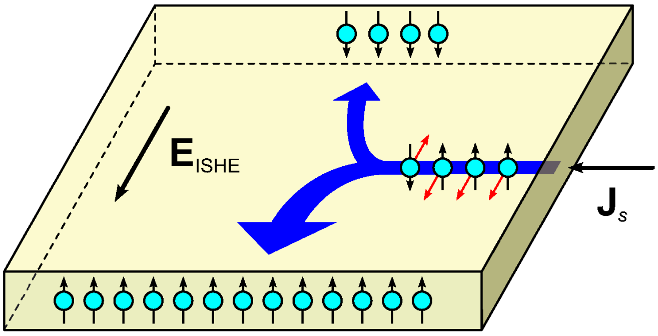

Figure 1.8: Schematic representation of the Spin Hall Effect Polarization, taken from [15]

Consider a heavy metal deposited on top of a ferromagnetic layer. A precessing magnetization in the ferromagnet will pump spins into the adjacent heavy metal. Due to the spin-orbit coupling the pumped spins are mixed to create a voltage known as an inverse spin hall voltage. Spin pumping phenomenon enhances the damping of the bilayer as the heavy metal acts as an effective spin sink leading to a faster decaying of the magnetization dynamics. Which is illustrated in 1.9.

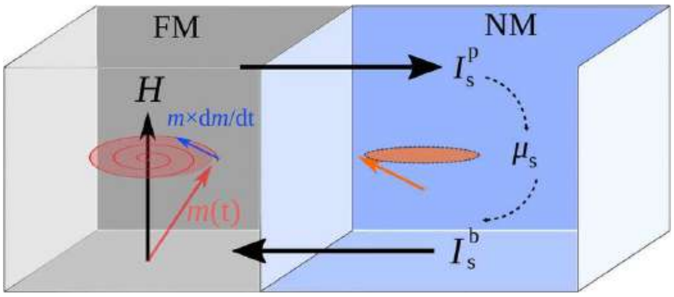

Figure 1.9: Spin Pumping Mechanism between a Ferromagnetic and a Non-magnetic interface, taken from [16]

Chapter 2

Experimental Procedure

In this chapter, we will discuss the experimental techniques that have been used during the thesis work. First, we will introduce the Pulsed laser deposition and the sputtering techniques that were used for the preparation of thin films. Second, we describe a homemade broadband ferromagnetic resonance experiment that was used to study the magnetization dynamics of the thin films. Then we end this chapter by discussing the scanning electron microscope (SEM) which is used for surface imaging, the Energy Dispersive Spectroscopy (EDX) for element specification, and finally the profilometer for the thickness measurements of the films.

2.1 Depositon Techniques

We used two different deposition techniques for thin film depositions, first the pulsed laser deposition (PLD) for the growth of magnetic thin films made of CoFe alloy and the sputtering for the deposition of the Platinum layer.

2.1.1 ***Pulsed Laser Deposition***

2.1.1.1 Description of PLD Setup

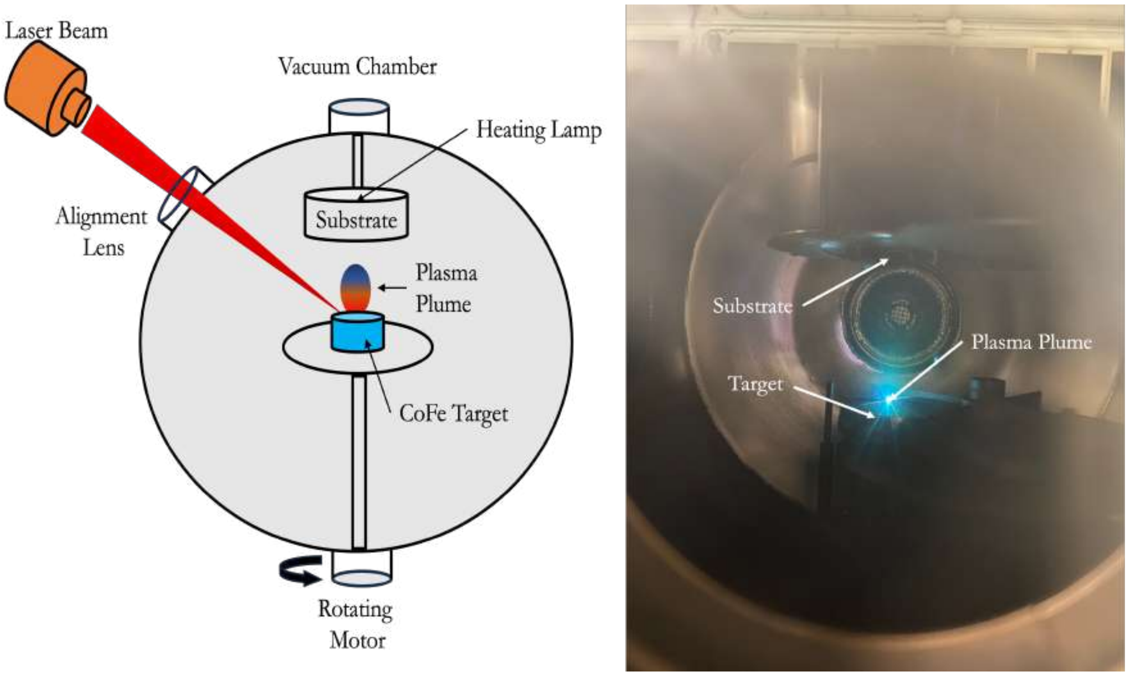

(a) (b)

Figure 2.1: (a) Schematic representation of the PLD setup. (b) Picture of the Plasma Plume created from the CoFe target

The Pulsed Laser Deposition (PLD) is a thin-film deposition technique that uses a high-intensity laser to ablate a certain material, in this case, we use a target of CoFe with a stoichiometry of 60% Co and 40% Fe. Then the ablated material is deposited onto an adjacent substrate forming a thin film. This method is widely used in various scientific and technological applications due to its precision and versatility. As seen in figure 2.1a, the PLD setup used at our facility consists of a vacuum chamber reaching pressures of $\approx 10^{-6}\ mbars$, a high energy laser beam generated by KrF gas with parameters $\lambda = 248nm, \tau = 20ns$. The laser energy can be varied up to 650 mJ with a repetition rate between [1-10 Hz]. It can house four targets sitting on a rotating platform. A substrate holder is directly placed above the target. A micrometer manipulator allows one to control the distance between the substrate and the target. The system is equipped with a lamp to control the temperature of an annealing process of the substrate which could increase up to $1000°C$.

In the thin film deposition process, silicon (Si) (100) wafers are initially prepared by cutting them into a square of $1cm \times 1cm$ and were cleaned with acetone, ethanol, and isopropanol. These cleaned substrates are then mounted on a holder using a rod, leaving a designated area free from deposition for subsequent thickness measurements. This is illustrated in figure 2.2. The alignment of the substrate to the target is critical and is achieved by placing the substrate orthogonally above the target while using a plexiglass disk for laser marking. The vacuum chamber is subsequently closed, and an ultra-high vacuum is established. The deposition phase involves activating the laser with varying energies on a rotating target, initially keeping the substrate shutter closed for around 3 minutes to clean impurities from the surface of the target. Then the shutter is open and the deposition starts for a finite time that is determined based on the desired thickness. After the deposition is done, the vacuum chamber is vented, and upon removal of the target and substrates, a noticeable discoloration appears on the substrate. This systematic approach ensures a consistent and controlled process for thin film preparation.

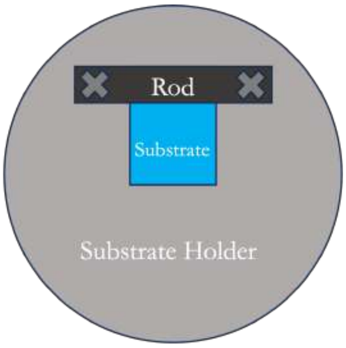

Figure 2.2: Illustrating the substrate when mounted on the holder of the PLD

2.1.2 *Sputtering*

We use the sputtering technique to deposit a layer of heavy metal of Platinum (Pt) on top of the CoFe layer to study the spin-pumping effect. The sputtering chamber setup is illustrated in Figure 2.3. Following the affixing of the film onto the substrate holder using carbon tape, the chamber undergoes a vacuum process reaching approximately 10^{-4} mbars. Subsequently, Argon gas is introduced into the chamber. Upon activation of the cathode node, the plasma is generated, and Pt atoms are deposited onto the substrate, forming a continuous layer. The machine halts automatically once the desired thickness is attained.

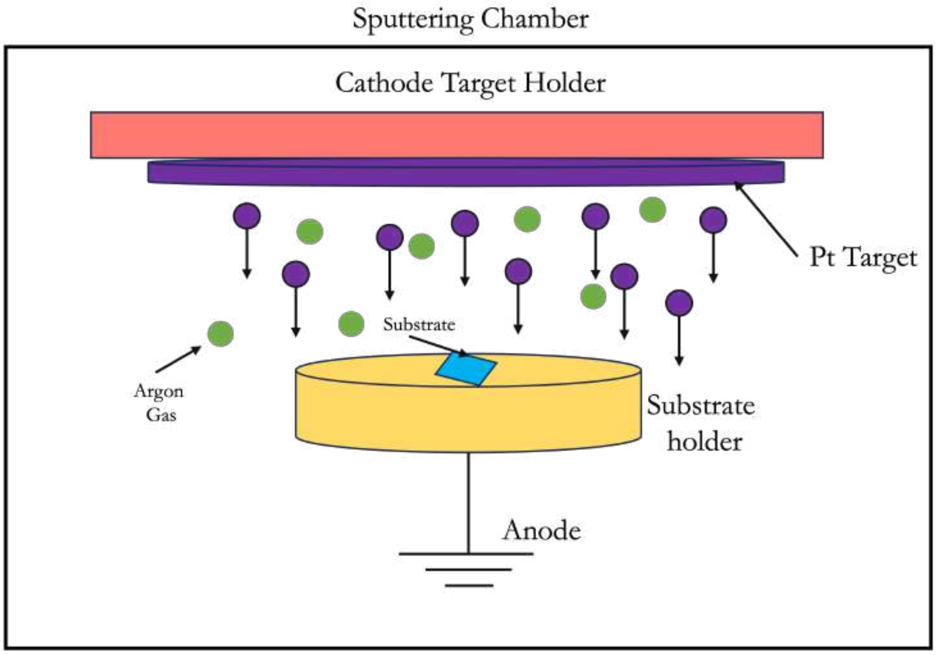

Figure 2.3: Schematic representation of the Pt sputtering apparatus

2.2 Broadband Ferromagnetic Resonance

The magnetic properties of the CoFe films are measured using a homemade broadband ferromagnetic resonance (B-FMR). This is a versatile technique that allows us to study the magnetization dynamics over a wide frequency range. This technique consists of two main components: (i) microwave excitation which is done using a coplanar waveguide (CPW) and (ii) signal detection using a lock-in amplifier. The block diagram above visualizes the FMR setup showing all the components.

2.2.1 *Setup Explanation*

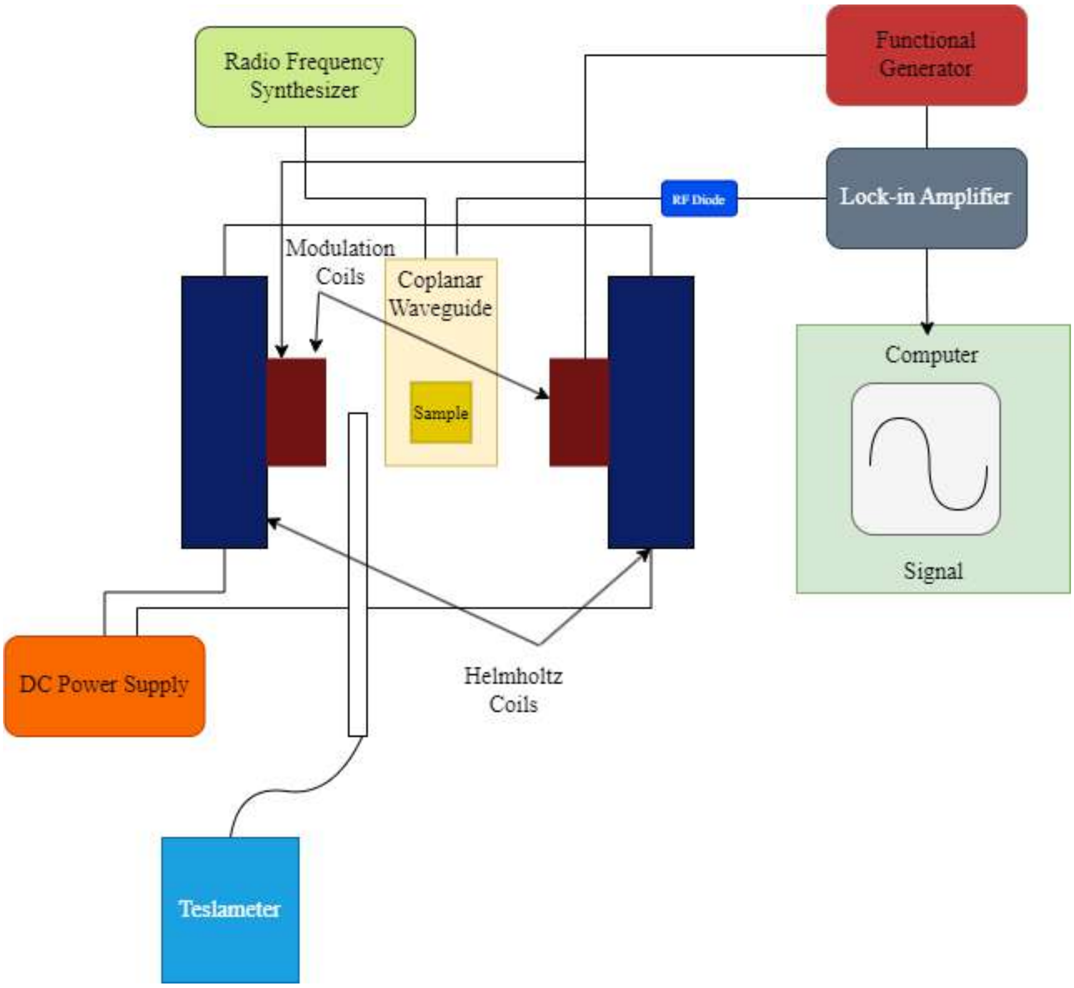

Figure 2.4: Schematic Representation of the BFMR setup using the Lock-in technique

2.2.2 *Microwave Excitations and Detection*

When a magnetic sample is placed under a magnetic field, its magnetization will align itself parallel to the field direction setting the equilibrium position of the magnetization. In the setup, we use large coils that are connected to a DC power supply and can produce a large IP field (H_{IP}) up to 0.7 T. As discussed above in section 1.3.4 and illustrated in figure 1.7, the magnetization will precess around the equilibrium direction once a small Radio Frequency (RF) field is applied perpendicular to the direction of the static field. In our setup, the excitation of the dynamics is done using a Coplanar Waveguide (CPW) where the sample is flipped over. The CPW has two ports and is designed to have very low microwave losses up to 40 GHz. It can excite waves with an infinite wavelength λ or zero wave number corresponding to the ferromagnetic resonance mode. The input port of the CPW is connected to an RF frequency synthesizer for the excitation. The frequency synthesizer can produce an RF frequency ranging from $10MHz$ to $19GHz$ with a variable input power between -20 dB to 20 dB. The resonance condition is achieved when the frequency of the magnetic oscillation in the films matches the RF frequency and a maximum absorption of the RF power is detected and the absorption will eventually decrease to zero away from the resonance condition. From the absorption curve, one can determine the resonance condition and subsequently extract the magnetic properties of the film. The second port of the CPW is connected to a lock-in amplifier for signal detection. An RF diode is connected between the second port and the lock-in amplifier used to amplify the signals. As we used a lock-in technique Helmholtz coils are used for modulation which are also connected to the lock-in at the reference channel. We modulate the signal at a low frequency of 860 Hz. The power supply and the lock-in amplifier are controlled using a Labview program.

2.2.3 *Measurement Procedure and Signal Analysis*

The ferromagnetic resonance measurement is carried out at a constant RF frequency while sweeping the static magnetic field. At the resonance condition, i.e. the matching between RF frequency and the ferromagnetic resonance frequency, a dip in the absorbed power is measured, an example of a resonance curve is plotted in figure 2.5 in black. As we have seen in the first chapter theoretically the resonance curve is described by a negative Lorentzian curve. In our setup, we detect the absorbed power using a lock-in technique. For this purpose, we connect the Helmholtz coil to a low-frequency function generator that provides a square wave signal of $860Hz$, with a small amplitude of the oscillating magnetic field $H_{\sim}$ of a few Oersteds. Therefore an additional AC modulation field, he^{iwt} is added on top of the static field, Where w is the frequency of the modulated field. Then the microwave signal includes the first two terms of Taylor's expansion:

$$\kappa(H + he^{iwt}) = \kappa(H) + iwhe^{iwt}\frac{d\kappa}{dH} \tag{2.1}$$

where the first component represents the microwave signal due to the DC field, this is primarily filtered out by the Lock-In amplifier. The Lock-In Amplifier measures the imaginary part of κ which is the derivative of the power with respect to the applied field, $\frac{dP}{dH}$. Therefore the signals that are detected in our setup are the measurement of the variation of the absorbed power as we change the magnetic field. Hence the detected curves resemble a derivative of a Lorentzain as shown in the red curve in 2.5. However, since the magnetic films are metallic, this causes an asymmetry in the Lorentzian curve related to the dispersion. To compensate for this effect we fit the FMR spectra with an asymmetric derivative of a Lorentzian which accounts for the absorption and dispersion. The equation that will govern our fit is represented as such:

$$\frac{-8A \cdot \Delta H^2 \cdot (H - H_{\text{res}}) + B \cdot \Delta H \cdot (\Delta H^2 - 4(H - H_{\text{res}})^2)}{(4(H - H_{\text{res}})^2 + \Delta H^2)^2} + C \cdot H + D \tag{2.2}$$

Where H_{res} is the midpoint between the two peaks, and ΔH is the line width of the curve i.e. the distance from peak-peak. This is illustrated in figure 2.5. The other parameters A and B are amplitude control parameters, and C and D are shifting parameters.

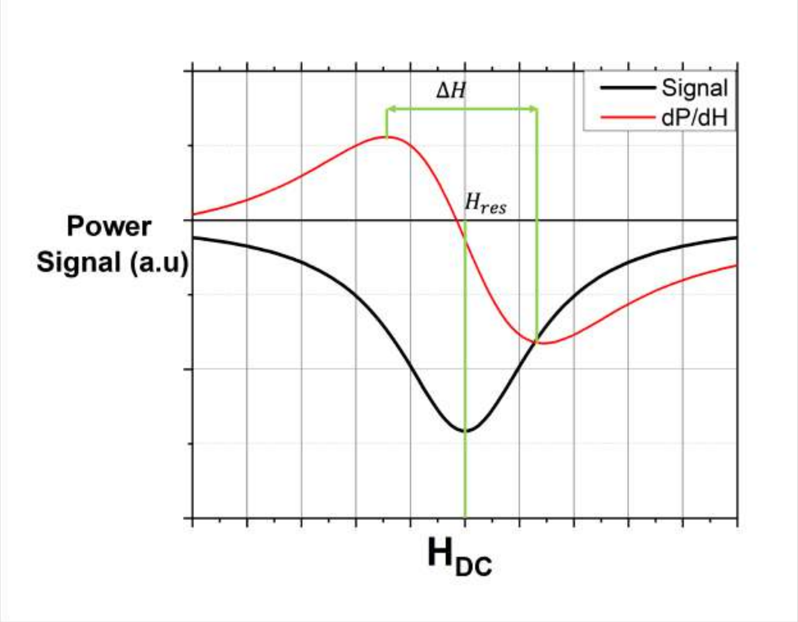

Figure 2.5: Power Signal at resonance, and its perspective derivative as a function of Magnetic Field Strength H

2.2.4 *Magnetic Field Calibration*

The flowing DC current in the coils produces a static magnetic field in our setup. We place a Tesla meter at the center of the coil to measure the conversion between the current and the generated magnetic field. The current is swept iteratively through the coils over a full range from -7A to 7A while we record the resulting magnetic field. The relation between the static field and the current is shown in figure 2.6 where we notice a linear relation between H_{DC} and I. The linear relationship is given by:

$$\mu_0 H(mT) = 61.2885\, I(A) + 7.7290 \tag{2.3}$$

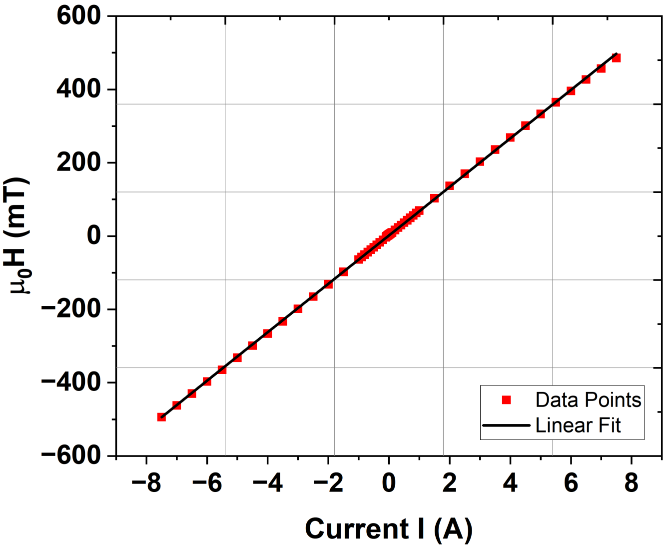

Figure 2.6: Measurement of the Magnetic Flux Density $\mu_0 H$ (mT) at the center of the CPW as a function of the Current I (A). Red line showing the linear fit

The value of the magnetic field at $I = 0$ represents the contribution of the remnant field of the poles.

2.3 Other Characterization Techniques

To check the quality i.e. the topology and the stoichiometry of the deposited layer, we employ scanning electron microscopy (SEM) and energy dispersive spectroscopy (EDX). While for the thickness a profilometer is used. Below we will discuss these techniques briefly.

2.3.1 *Scanning Electron Microscope (SEM)*

An SEM is a powerful imaging instrument used in various scientific and industrial fields for high-resolution imaging of surfaces. Unlike optical microscopes that use light to magnify images, SEMs use a focused beam of electrons to achieve much higher resolution. Figure 2.7 shows the working principles of the SEM along with the machine that will be used.

The SEM will be used to study the film's topology. This way one can measure the size and diameter of the metallic CoFe droplets that were deposited on the substrate via the PLD along with their quantity and how close or far off they are spaced. Since CoFe is already conducting, the SEM will show a clear image of the droplets without needing to sputter on any conducting layer.

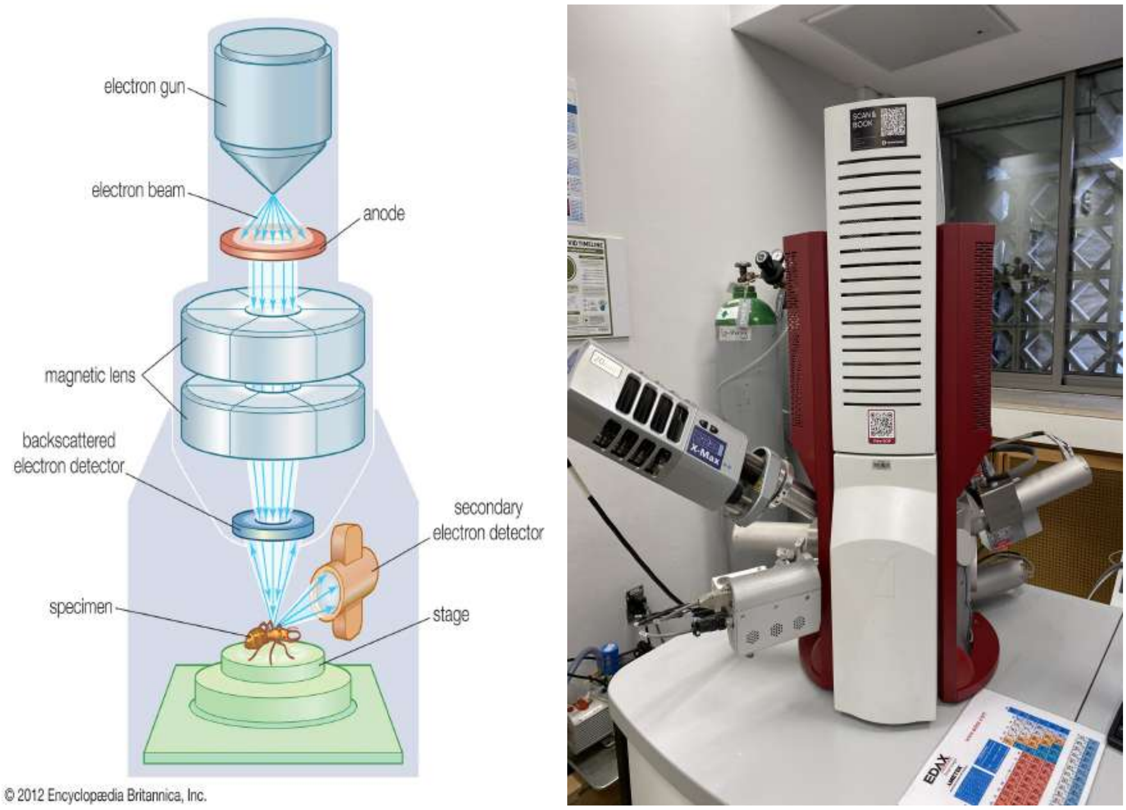

© 2012 Encyclopædia Britannica, Inc.

(a) (b)

Figure 2.7: (a) Schematic representation of the working principle of the SEM. (b) Picture of the SEM machine used in our experiment

2.3.2 *Energy Dispersive X-ray (EDX)*

Energy Dispersive X-ray (EDX), also known as Energy Dispersive X-ray Spectroscopy (EDS) or Energy Dispersive X-ray Analysis (EDXA), is a technique used in conjunction with electron microscopes to analyze the elemental composition of a sample. EDX provides information about the characteristic X-rays emitted by a material when it is irradiated with a high-energy electron beam. The energy-dispersive detector generates a spectrum that represents the intensity of X-rays at different energy levels. Each peak in the spectrum corresponds to a specific element in the sample. By analyzing the peaks in the spectrum, one can determine the elemental composition of the sample. The position and intensity of the peaks provide information about the types and amounts of elements present.

By measuring the atomic percentage of the film, one can measure the concentration of Co and Fe and compare them with the target. This way one can draw a connection between the atomic stoichiometry of the film and its perspective magnetic properties.

2.3.3 *Surface Level Profilometer*

A surface profilometer, or surface profiler, is an instrument used to measure the three-dimensional (3D) profile of a surface. It provides information about the thickness, surface roughness, and texture. Surface profilometry is crucial in various fields, including materials science, engineering, and manufacturing, where the surface quality of a material or product is essential.

The one that will be used in this experiment is a contact profilometer. These instruments use a stylus or a probe that physically contacts the surface to measure its profile. The stylus moves along the surface, and the vertical movement is recorded to create a profile. As shown in figure 2.8, the stylus starts on the substrate and moves up towards the CoFe layer. The vertical step height is recorded by the software and is registered by the perspective thickness of the film.

Figure 2.8: Drawing representing the mechanism of the Surface Level Profilometer *Not to Scale*

Chapter 3

Results & Analysis

3.1 Introduction

The importance of magnetic damping is critical for devices utilizing the electronic spin degree of freedom, impacting energy requirements and operational speed. However, in common ferromagnetic materials, the Gilbert damping remains high in the order of 10^{-2}. This challenge hinders various applications in spintronics and spin-orbitronics, particularly those reliant on materials with ultra-low damping [17], [18]. The conventional belief is that the high damping in metallic ferromagnets is dominated by the scattering of magnons by conduction electrons. On the contrary, Heusler alloys and magnetic insulators have shown extremely low damping coefficients below 10^{-4} due to the absence of conduction electrons [19], [20]. Despite their low damping yet, the growth of these materials is very challenging and they are not compatible with the CMOS technology. However, recent works show that cobalt and iron binary alloys challenge this limitation and show a relatively low damping coefficient. Indeed, theoretical predictions proposed by Mankovsky et al.[13] showed a damping coefficient of 5×10^{-4} could be achieved in $Co_{20}Fe_{80}$ due to a unique band structure, featuring a sharp minimum in the density of states at the Fermi level, corresponds to the alloy concentration where the minimum magnetic damping occurs. Later, Schoen et al. [21], [22] carried out a detailed study and showed indeed a minimum damping in $Co_{20}Fe_{80}$ alloys confirming the theoretical predictions.

In this chapter, we aim to study the magnetization dynamics of $Co_{60}Fe_{40}$ thin films prepared by the PLD. Our first aim is to achieve high-quality nanometer-thin films. To achieve this we study the characteristics of CoFe films prepared at different deposition parameters where we vary the laser energy and the temperature. Once the optimal deposition is determined, we perform a thickness dependence study where the thickness of the CoFe layer is varied between 10 and 25 nm. Finally, we study the spin-pumping effect in bilayers of CoFe/Pt where we varied the thickness of the Pt layer to calculate the spin diffusion length in Pt. This systematic study will be useful for magnonics, spintronic, and spin Hall devices.

3.2 Variation of Growth Parameters

In this study, we prepared films in the following series:
S1 series: This series aims to find the best deposition temperature of the CoFe films. To achieve this, the films were prepared at different deposition temperatures ranging from 300K to 573 K. These films were grown at similar deposition parameters where the laser energy is 400 mJ, with a repetition rate of 10 Hz and the deposition time is 90 mins resulting in a film thickness of $\sim 20nm$.
S2 series: This series aims to study the thickness dependence study and achieve good films with a nanometer range. We vary the laser energy between 300 mJ and 450 mJ resulting in film thicknesses between 10nm and 25 nm.
S3 series: This series aims to study the spin-pumping effect in CoFe/Pt bilayers, where a Pt layer is deposited with different thicknesses ranging between 0-6 nm.

3.3 Thin Film Characterization

In this section, we will discuss the surface imaging of thin films that is done using scanning electron microscopy, the stoichiometry of the deposited layers using EDX, and the film thickness using the profilometer.

3.3.1 ***SEM and EDX Results of the Films***

3.3.1.1 Surface Imaging

Figure 3.1 shows the film being held vertically to show a side profile of it. The bright small layer on the substrate shows the deposited CoFe layer.

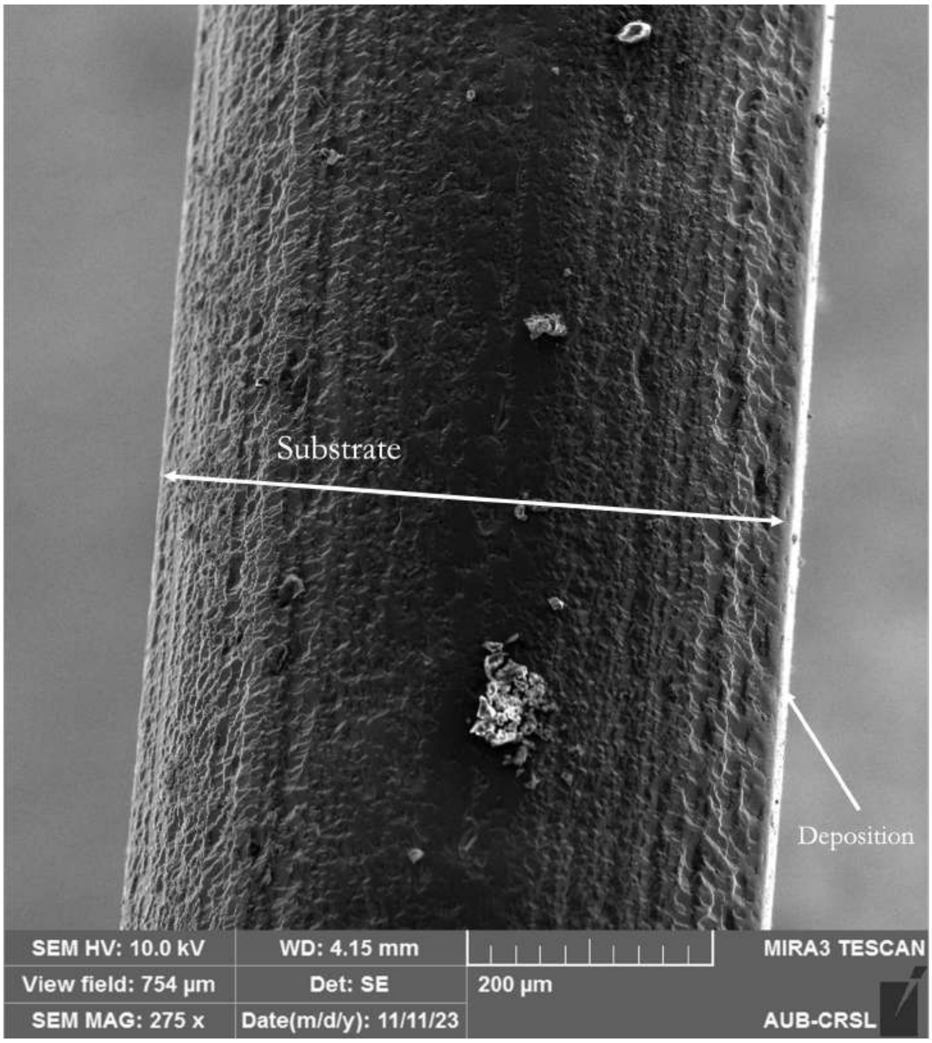

Figure 3.1: Vertical alignment of the film showing the crossectional side of the substrate and the perspective deposited film

Figure 3.2: A Reference sample help vertically under the SEM

The growth of metallic films using the PLD technique is usually associated with the formation of droplets on top of the surface. We used the SEM to look into the formation of droplets or islands on the surface of the magnetic films and check their formation at different growth conditions. Figure 3.3, shows images taken for samples grown at different laser energy between [300-500 mJ]. One can observe discontinuous droplets which spread over the film surface. The radius of these droplets varies with the laser energy. We report a general increase in the droplet size with the increase of the laser energy. For example, the droplet size is around $\approx 270nm$ at 300 mJ and it increases to $\approx 1800nm$ for films prepared at 450 mJ i.e. by a factor of 6. Whilst in films prepared with lower laser energies the films look more continuous where droplets are unevenly distributed.

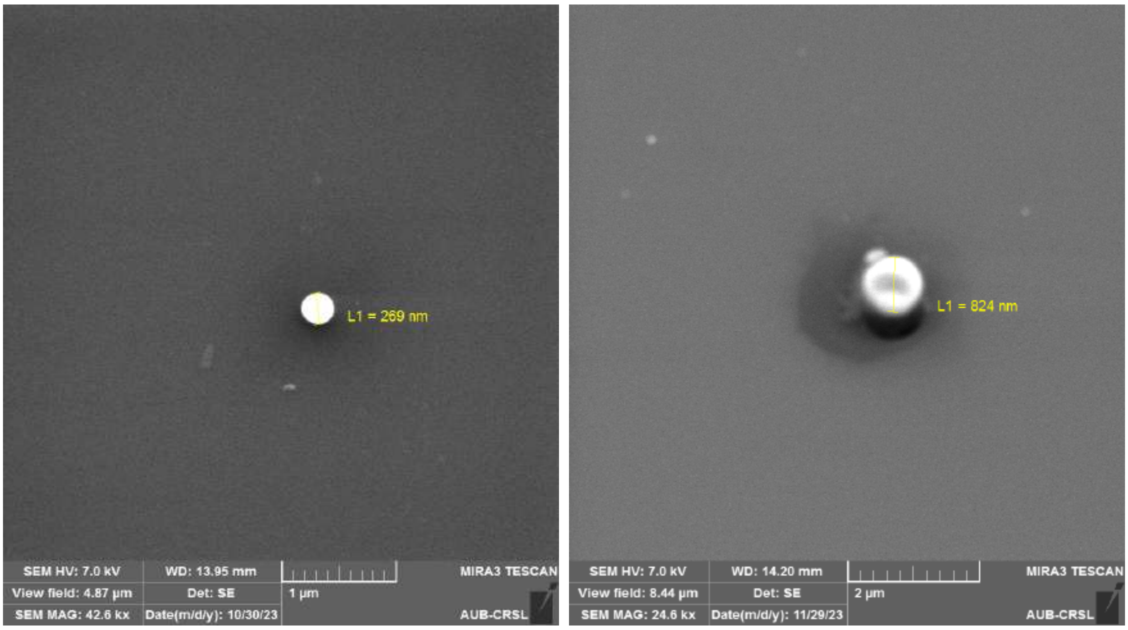

(a) Film at Laser Energy 300 mJ (b) Film at Laser Energy 400 mJ

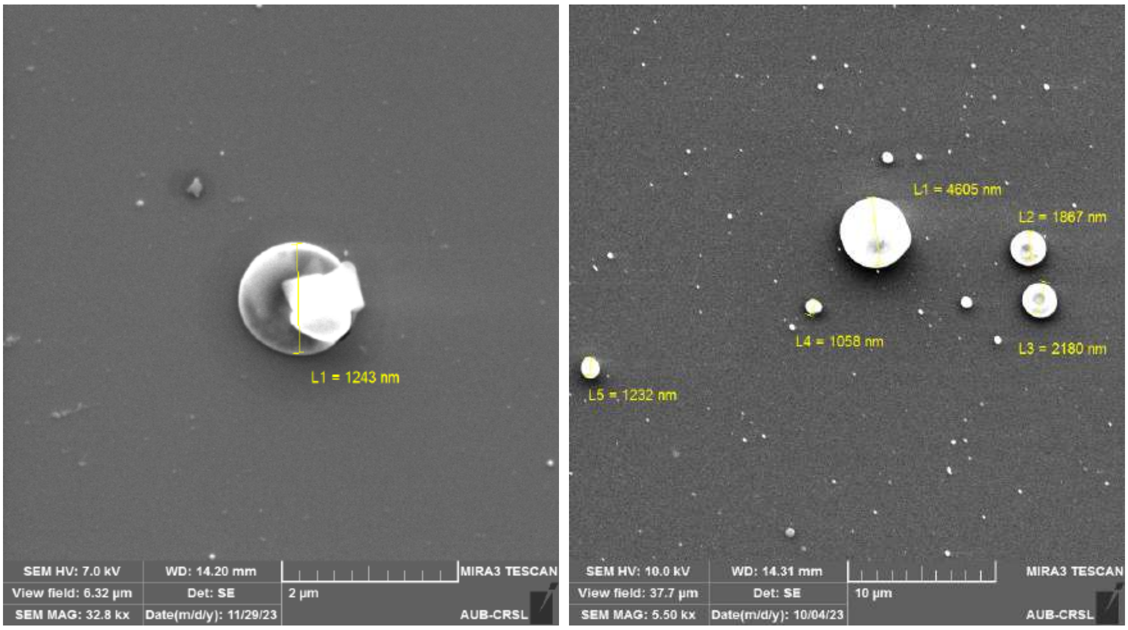

(c) Film at Laser Energy 450 mJ (d) Film at Laser Energy 500 mJ

Figure 3.3: Progressively increasing CoFe droplet sizes as a function of Laser Energy

3.3.1.2 Atomic Composition

The stoichiometry of the films is measured using the EDX equipped with the SEM. After scanning a large area of $1 \times 1mm^2$, we measured the composition of Co-Fe within this area and we repeated this for different regions. An example of the EDX results is shown in 3.4, where several peaks are detected that are mainly the Si related to the substrate and the Co and Fe atoms representing the film. The sample shows that the atomic composition is roughly 66 % of Co and 34 % of Fe which resembles the the target composition as shown in 3.5. We perform EDX measurements for all samples of S1 and S2 series. We notice that the atomic composition is weakly affected by the deposition temperature or the film thickness. In general, we can conclude that the change in the stoichiometry of the films is marginal around 65 % of Co and 35 % of Fe as shown in figure 3.6.

3.4.

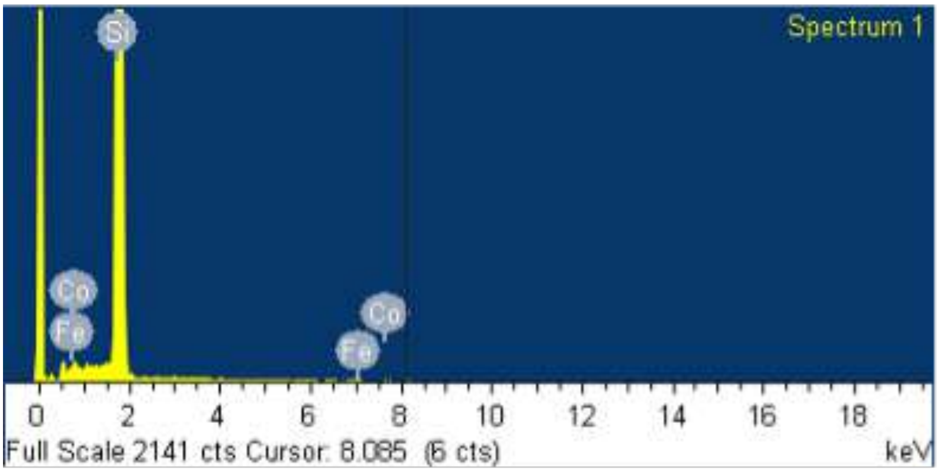

Figure 3.4: EDX intensity spectrum with their perspective atomic composition

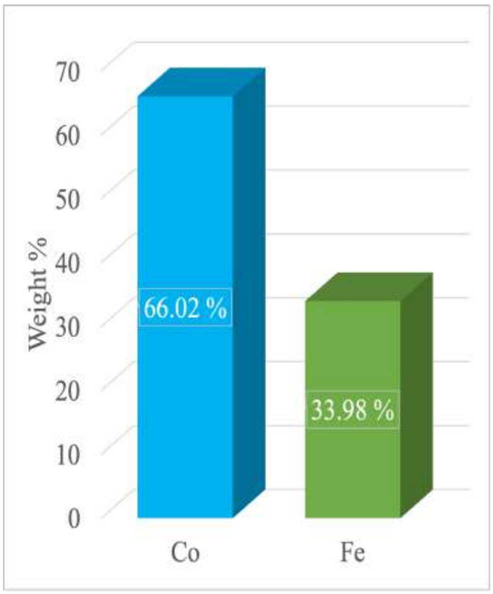

Figure 3.5: Quantitative results for the Atomic % of the sample from the EDX

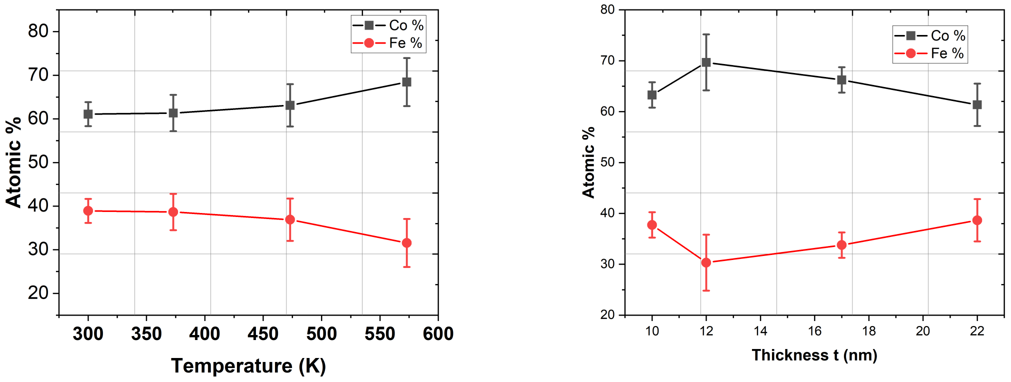

(a) Atomic % of the S1 Series (b) Atomic % of the S2 Series

Figure 3.6: EDX of S1 and S2 films

3.3.2 *Thickness Measurements*

The thickness measurement is done using the profilometer. As the stylus is stationed on the substrate and moves above the film, a step height is seen which represents the thickness of the sample. Two examples are shown below for samples of thicknesses 13 and 10 nm figure 3.7. One can notice a sharp increase in the step height when the stylus jumps over the CoFe film. In this work, the thickness of the films is measured using a profilometer.

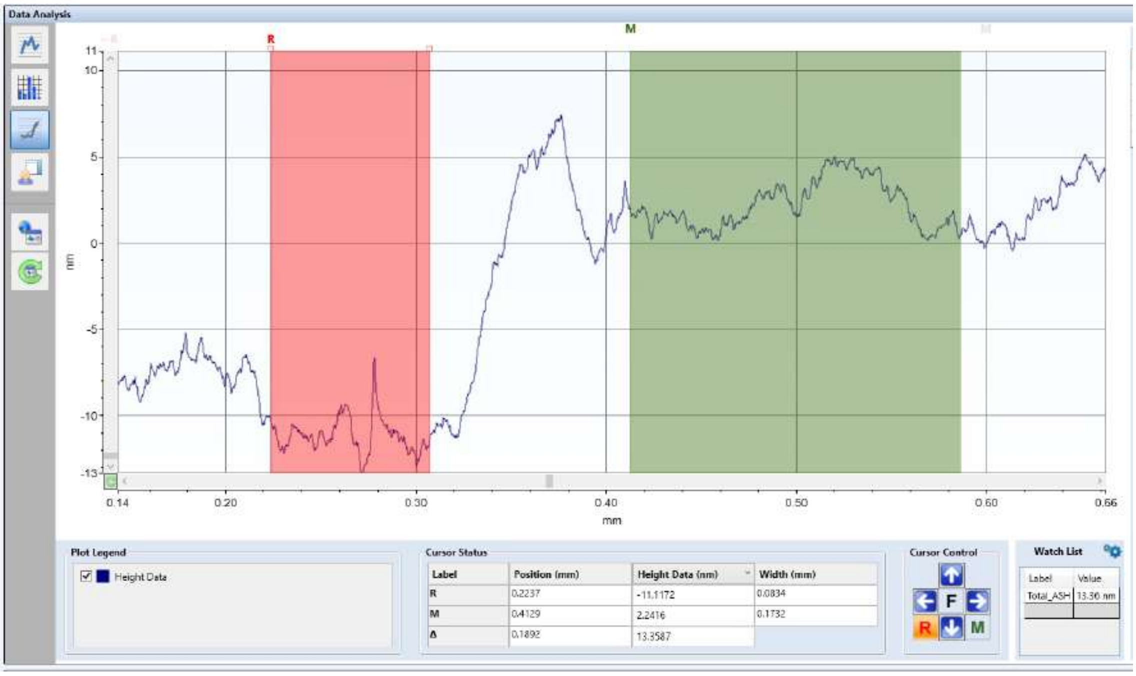

Label	Position (mm)	Height Data (nm)	Width (mm)
R	0.2237	-11.1172	0.0834
M	0.4129	2.2416	0.1732
Δ	0.1892	13.3587	

Label	Value
Total_ASH	13.36 nm

(a) Profilometer step height of a sample with thickness 13 nm

Label	Position (mm)	Total Profile (nm)	Width (mm)
R	0.3088	-9.6198	0.0676
M	0.5384	0.6866	0.0790
Δ	0.2297	10.3064	

Label	Value
Total_ASH	10.31 nm

(b) Profilometer step height of a sample with Thickness 10 nm

Figure 3.7: Surface Level Profilometer Results

3.4 Broadband FMR Analysis

As we have discussed in section 2.2, the magnetic properties of the magnetic films are determined using a broadband FMR setup. Our measurement procedure is that we set a constant microwave frequency ranging between 4 and 19 GHz while we sweep the magnetic field $\mu_0 H$ at each frequency. Using the lock-in amplifier we measure the change of the absorbed power with respect to the field ($\frac{dP}{dH}$) vs. $\mu_0 H$ as shown in 3.8. We fit these signals with an antisymmetric Lorentzian function from where we extract the resonance field ($\mu_0 H_{res}$) and the full width at half maximum (FWHM) ($\mu_0 \Delta H$).

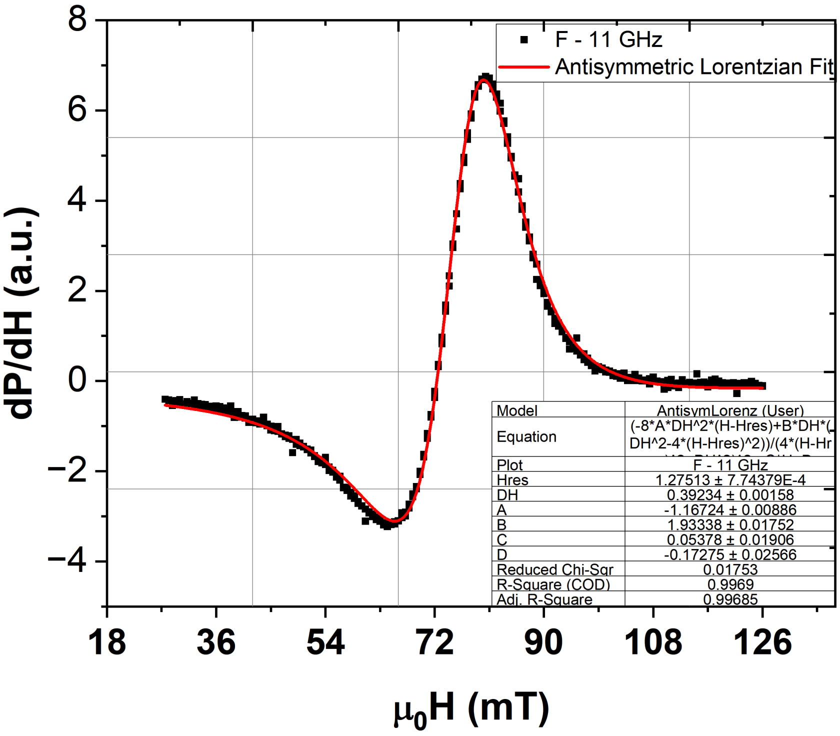

Model	AntisymLorenz (User)
Equation	(-8*A*DH^2*(H-Hres)+B*DH*(DH^2-4*(H-Hres)^2))/(4*(H-Hr
Plot	F - 11 GHz
Hres	1.27513 ± 7.74379E-4
DH	0.39234 ± 0.00158
A	-1.16724 ± 0.00886
B	1.93338 ± 0.01752
C	0.05378 ± 0.01906
D	-0.17275 ± 0.02566
Reduced Chi-Sqr	0.01753
R-Square (COD)	0.9969
Adj. R-Square	0.99685

Figure 3.8: $\frac{dP}{dH}$ Signal as a function of $\mu_0 H$ with an Antisymmetric Lorentzian Fit in red

A full spectrum of the resonance curves measured at an input power of 10 dB and for 6–19 GHz frequencies for a single sample are shown in figure 3.9. Note that the resonance curves shift to higher magnetic fields as the frequency increases. This mode correspondence to the FMR mode. The amplitude of the FMR-peaks varies at each frequency due to the microwave losses within the microwave circuit (CPW, cables, rf-diode, etc..). We analyze each curve independently to extract $\mu_0 H_{res}$ and $\mu_0 \Delta H$ as summarized in the table 3.1.

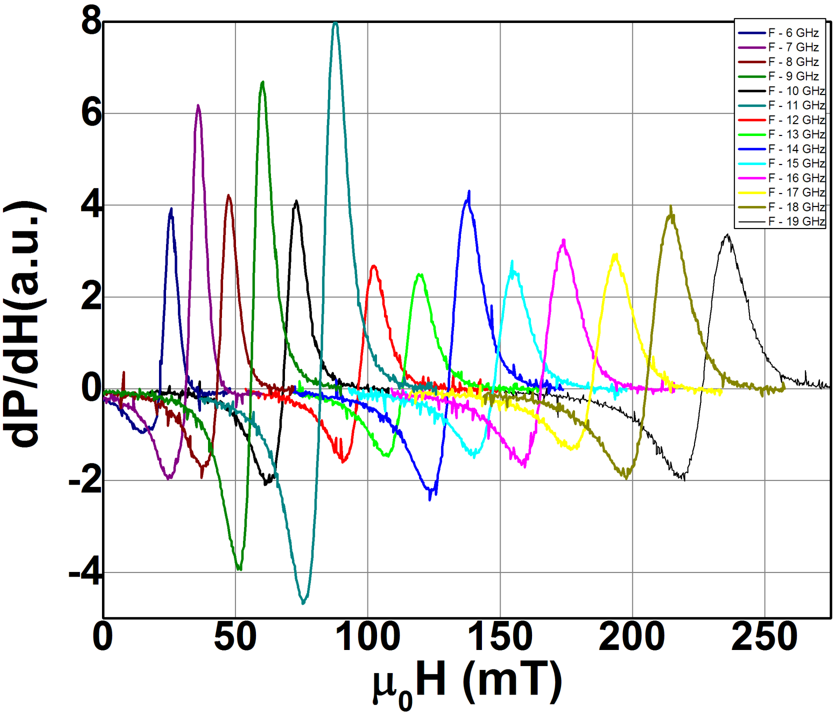

Figure 3.9: Full signal spectrum of all permissible frequencies for a reference sample

Frequency (GHz)	$H_{res}(mT)$	$\Delta H(mT)$
6	31.78242	27.42605
7	40.68007	28.52325
8	50.26532	28.68306
9	60.7947	30.35642
10	72.97478	30.8542
11	85.80327	31.75181
12	100.42268	33.43313
13	115.34517	35.17017
14	130.86218	36.62433
15	146.67431	40.02677
16	160.57858	38.6669
17	178.02672	39.76655
18	196.8329	41.78401
19	215.42723	42.94184

Table 3.1: FMR analysis of a reference sample

The injected power improves the signal-to-noise ratio (SN) during the excitation of the FMR mode in thin films. While we aim to improve the SN ratio, we ensure to excite the linear mode and avoid excitation of non-linear dynamics. For each sample at a single frequency, we do acquisition at several injected power between [-20 and 20 dB] as shown in 3.10. Note that with the increase of the injected power H_{res} and ΔH remain constant. Thus the power of the RF field doesn't interfere with the experimental data. Note that, for consistency for each sample the full spectra are done at a single, same input power at all frequencies.

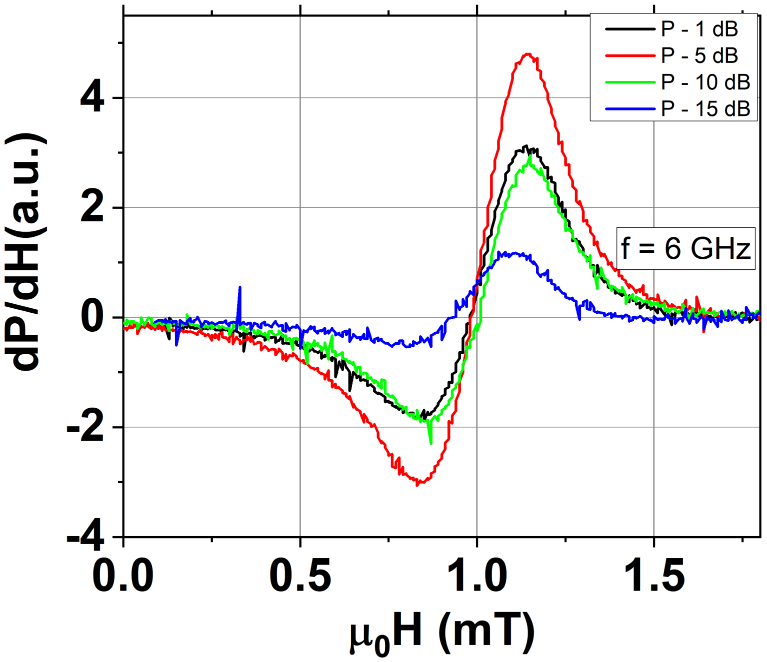

Figure 3.10: Reference signal measured over 4 different powers of the RF synthesizer

For each film, we extract the saturation magnetization M_s from the plot of the frequency vs. $\mu_0 H_{res}$ as shown in 3.11, and by fitting it to Kittel's equation:

$$f = \frac{\gamma}{2\pi}\sqrt{(\mu_0 H_{res})^2 + (\mu_0 H_{res})(\mu_0 M_S)} \tag{3.1}$$

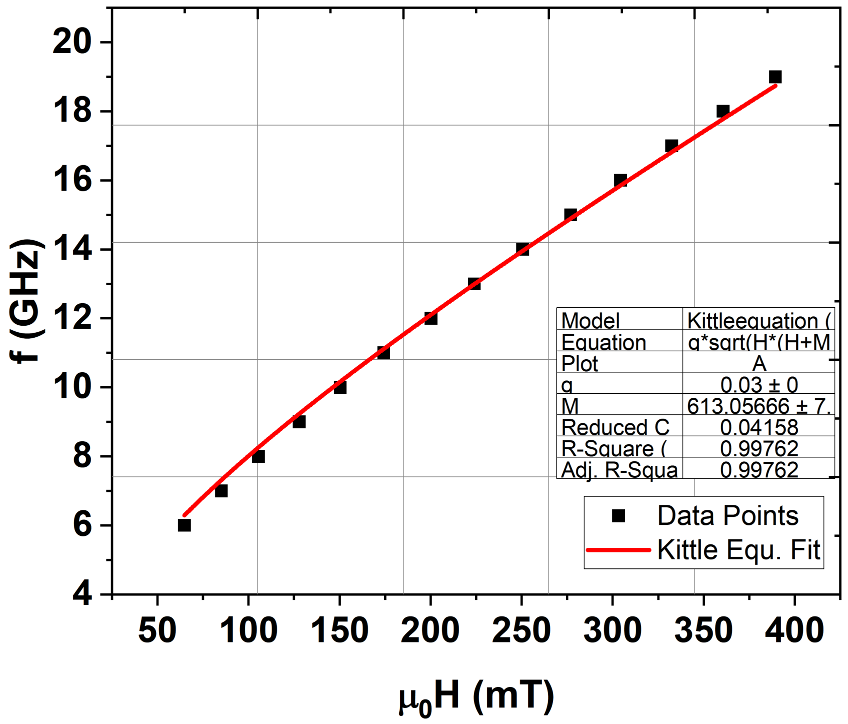

Figure 3.11: Plot representing the data points in black and the Kittel Equation fit in red

By following the full width at half maximum ΔH vs. the frequency as shown in 3.12, the Gilbert damping α of the films is extracted using

$$\mu_0 \Delta H = \frac{4\pi\alpha}{\gamma} f + \mu_0 \Delta H_0 \tag{3.2}$$

where α is the total intrinsic damping calculated from the slope and while the inhomogeneous broadening $\mu_0 \Delta H_0$ is extracted from the y-intercept.

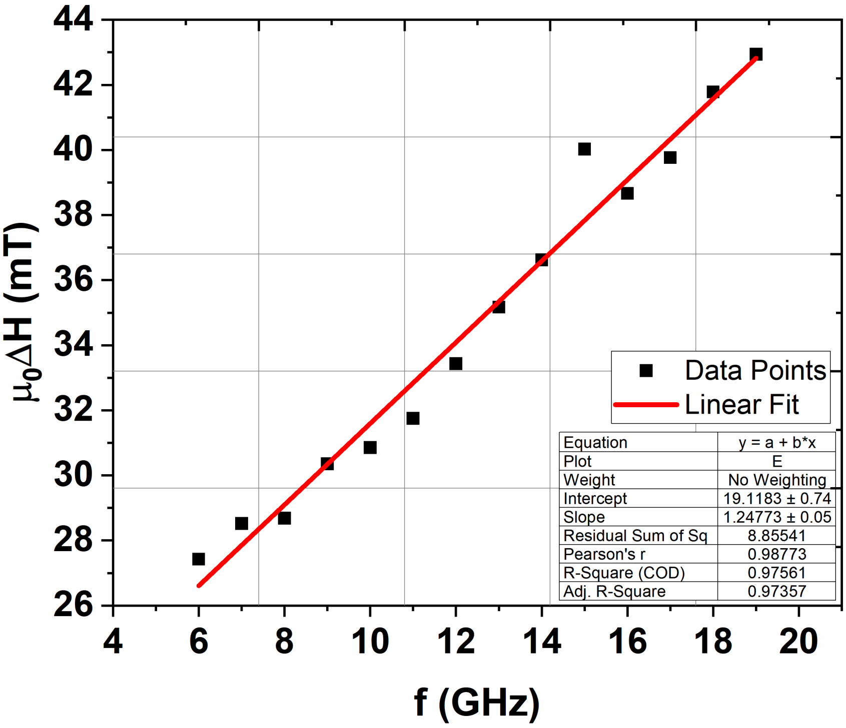

Equation	y = a + b*x
Plot	E
Weight	No Weighting
Intercept	19.1183 ± 0.74
Slope	1.24773 ± 0.05
Residual Sum of Sq	8.85541
Pearson's r	0.98773
R-Square (COD)	0.97561
Adj. R-Square	0.97357

Figure 3.12: Variation for FWHM as a function of RF frequency and the linear fit in red

3.4.1 *Radiative Damping*

An additional factor contributing to damping is the inductive interaction between the Coplanar Waveguide (CPW) and the sample, known as radiative damping. The value of α_{rad} is directly influenced by the coupling between the magnetic film and the CPW and can be reasonably approximated using the formula proposed by Schoen et al. [23]:

$$\alpha_{rad} = \frac{\gamma M_S \mu_0^2 tl}{16 Z_0 w_{cc}} \tag{3.3}$$

Here, γ represents the gyromagnetic ratio, M_S is the saturation magnetization, μ_0 is the magnetic permeability, t is the thickness of the thin film, l is the sample length, $w_{cc} = 200\mu m$ is the width of the CPW, and $Z_0 = 50\Omega$ is the impedance. For precise Gilbert damping measurements, we computed the radiative damping for each film and subtracted it from the total damping: $\alpha_G = \alpha_{tot} - \alpha_{rad}$, as elaborated later.

It is important to highlight that the contribution to damping from eddy currents [24] is negligible in our films due to their thickness of 50, nm; hence, eddy currents do not play a noticeable role in α_G.

3.5 S1 Series - Effect of Deposition Temperature on the Film Quality

As a first step in growing CoFe films, we search for the optimal deposition temperature at which we could achieve magnetic thin films with good and reproducible quality. We grow a series of S1 films in which we vary the deposition temperature between 300 -580 K where all samples were deposited with a laser energy of 400 mJ for 90 minutes. Once the desired temperature is attained, deposition takes place. By the end of the deposition, films are annealed at the set temperature for an additional two hours. Subsequently, the sample is cooled overnight under a vacuum to prevent oxidation of the CoFe film. As previously mentioned the film thickness is around 20 nm and the atomic composition is weakly dependent on the temperature as summarized in.

Sample	Substrate	Temp (K)	Thickness (nm)	Co %	Fe %	Spectrum
S6	Si	573 K	20 nm	68.45	31.55	A.1a
S7	Si	473 K	18 nm	63.11	36.89	A.1b
S9	Si	373 K	22 nm	61.35	38.65	A.2a
S10	Si	300 K	21 nm	61.09	38.91	A.1d

Table 3.2: Growth parameters and film characteristics of S1 Series films under varying annealing temperatures

The magnetic properties of S1 samples are extracted following the same procedure as discussed above. Figure 3.13a shows the variation of the f vs. $\mu_0 H_{res}$ and the FWHM vs. frequency for samples prepared at different temperatures along with the respective fits.

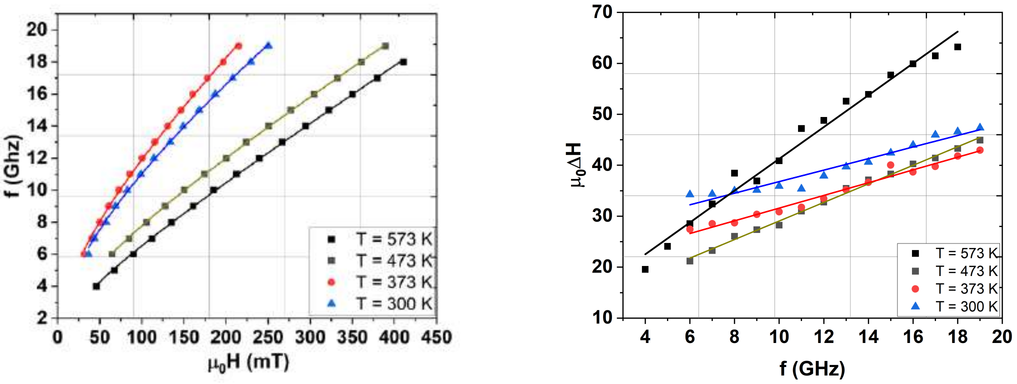

(a) Frequency-field dependence

(b) FWHM vs. frequency

Figure 3.13: BFMR Results of the S1 Series along with corresponding fits

Sample	Temperature [K]	$\mu_0 M_S$ [T]	α_G	$\mu_0 \Delta H_0$ [T]
S6	573	0.483	0.0468	0.0100
S7	473	0.613	0.0273	0.0108
S9	373	1.542	0.0184	0.0164
S10	300	1.297	0.0170	0.0255

Table 3.3: Perspective magnetic properties of the S1 Series

Figure 3.14 shows the variation of the M_S with the deposition temperature (T_{dep}). We note an increase in M_S as the T_{dep} increases forming a peak around 373 K with M_S of 1.6 T and decreasing to 0.5 T at higher temperatures. A low M_S of 0.5 T is also measured for films prepared at high temperatures with higher laser energy of 550 mJ. Liu et al. [25] also noted a similar correlation between magnetization and deposition temperature. This relationship is ascribed to lattice structure disorder, potentially resulting in a mixed regime between BCC and FCC structures [22], [26]–[28].

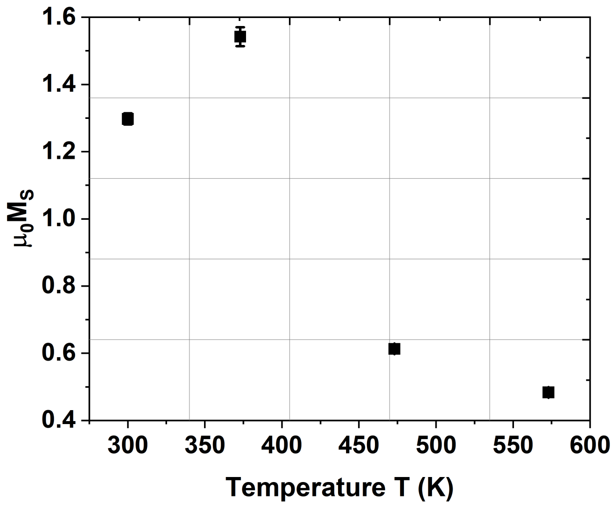

Figure 3.14: Variation of the M_S as a function of the annealing temperatures

Figure 3.13b shows the variation of the Gilbert damping vs. the T_{dep}. We note a large increase of the damping from 0.017 to 0.047 as the temperature increases from 300 to 573 K. This could be thermal disturbances and phase transitions at higher temperatures causing misalignment and disorders to the relative magnetic moments.

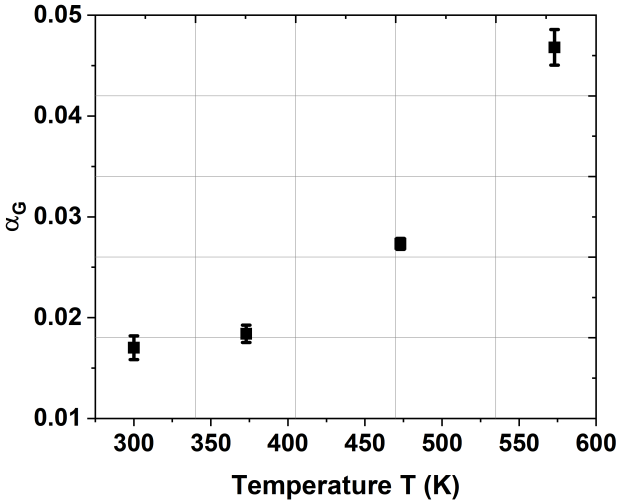

Figure 3.15: Variation of α_G as a function of the annealing temperatures

We conclude room temperature is an appropriate deposition temperature that allows us to achieve films with high magnetization and low Gilbert damping. We achieve magnetic films with a value of M_S similar to the bulk value, around 1.6 T, and a reasonable value of the Gilbert damping α_G although it deviates from the bulk value by a factor of 2. Which is similar to what was predicted in Thonig et al. [11].

Finally, we note a significant reduction in inhomogeneous broadening, $\mu_0 \Delta H_0$, with increasing deposition temperature, as depicted in Fig. 3.16. Specifically, $\mu_0 \Delta H_0$ decreases from 0.02546 T to 0.01005 T over the temperature range of 300 to 570 K suggesting that the films prepared at elevated temperatures are magnetically more homogeneous than films grown at lower temperatures.

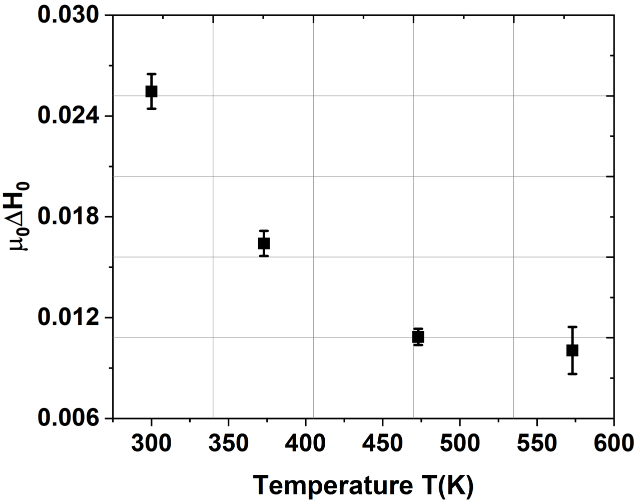

Figure 3.16: Inhomogeneous Linewidth Intercept $\mu_0 \Delta H_0$ as a function of annealing temperatures

3.6 S2 Series - Effect of Film Thickness

In this thesis, we aim to grow magnetic films with a nanometer thickness using the PLD technique. For this purpose, we prepared a S2 series of films with different thicknesses ranging between 10 and 22 nm. We grow these films at room temperature while we changed the laser energy between 300 and 440 mJ and annealed them during deposition and 120 minutes after deposition at $T_{dep} = 373K$, as summarized in 3.4

Sample	Substrate	Energy (mJ)	Thickness (nm)	Co %	Fe %	Spectrum
S9	Si	440	22	61.35	38.65	A.2a
S11	Si	400	17	66.23	33.77	A.2b
S12	Si	350	12	69.67	30.33	A.2c
S13	Si	300	10	63.27	37.73	A.2d

Table 3.4: Growth parameters and film characteristics of S2 Series films under varying thicknesses

The magnetic characteristics of S2 samples are determined using the same procedure as discussed above and are summarized in 3.2. Figure 3.20 shows the full range of experimental data extracted from the broadband FMR measurements for all films. It shows the frequency-field dependence and the change of the FWHM vs. frequency along with the corresponding fits.

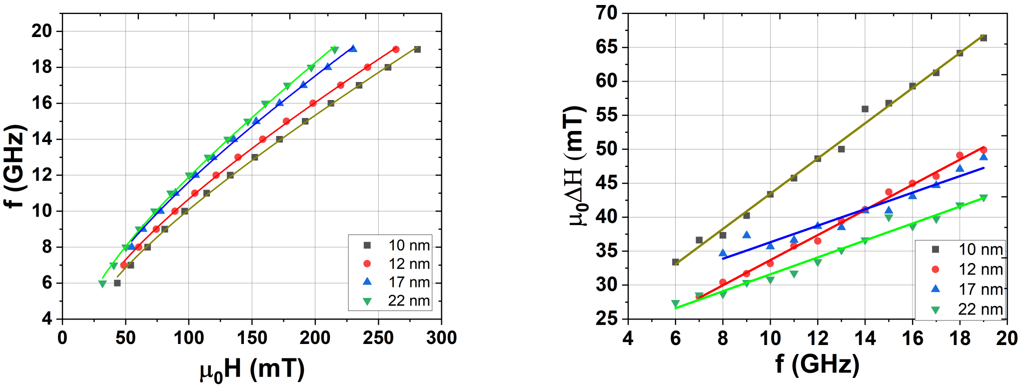

(a) Frequency-field dependence

(b) FWHM vs. frequency

Figure 3.17: BFMR Results of S2 Series along with corresponding fits

Sample	Thickness (nm)	$\mu_0 M_S$ (T)	α_G	α_{rad}	$\mu_0 \Delta H_0$ (T)
S9	22	1.544	0.017	6.31×10^{-4}	0.0191
S11	17	1.458	0.018	4.61×10^{-4}	0.0241
S12	12	1.213	0.0275	2.71×10^{-4}	0.0152
S13	10	1.092	0.0387	2.03×10^{-4}	0.0175

Table 3.5: Perspective magnetic properties of S2 Series Samples

Using the Kittel fits, we extract M_s vs. thickness as shown in Fig. 3.18. We measure an increase of M_s with the film thickness. It increases from about 1.1 T to 1.55 T as the thickness varies from 10 to 22 nm. For thick films, M_S approaches the bulk saturation magnetizations. The reported trend of M_s vs. t is in agreement with other studies Yan et al. [29], Ranjbar et al. [30], and Belmeguenai et al. [31].

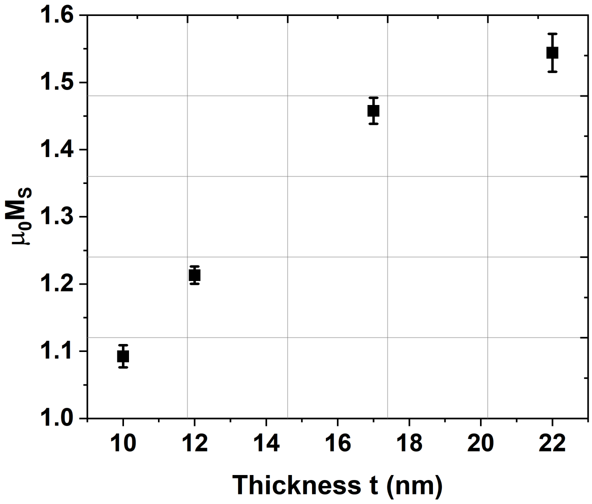

Figure 3.18: Variation of $\mu_0 M_S$ vs. the thickness t of the Sample

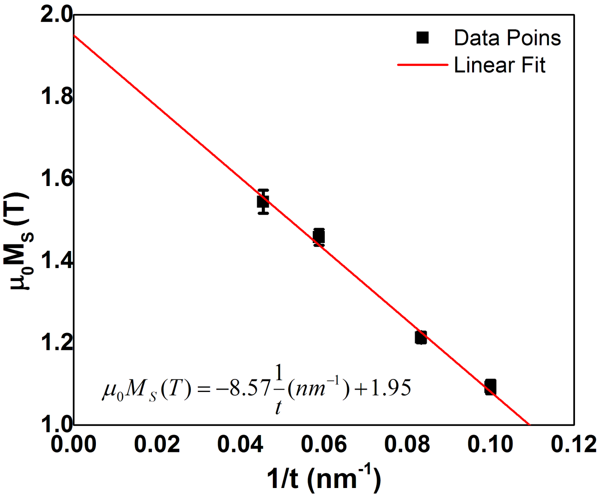

Figure 3.19: Variation of the $\mu_0 M_S$ vs. the inverse Thickness $\frac{1}{t}$ of the sample. Red line representing the linear fit

Figure 3.19 illustrates the relationship between magnetization and inverse of the film thickness $\frac{1}{t}$, which is governed

$$\mu_0 M_S = -8.57 \times 10^{-9} \times \frac{1}{t} + 1.95 \tag{3.4}$$

Where M_s and t are measured in Tesla and meters, respectively. Extrapolating this relationship to infinity, representing the bulk regime, results in M_S approaching 1.95 T. This value aligns closely with the predicted magnetization value for $Co_{60}Fe_{40}$ [32]. Considering the saturation magnetization of Co and Fe, approximately 1.75 T and 2.22 T respectively, one can calculate an expected magnetization value to the first order, yielding approximately 1.938 T.

Additionally, the slope is $\propto$ to $\frac{H_k}{\mu_0 M_S}$ the surface field anisotropy factor. This field is due to surface effects. In addition to the dipolar in-plane field, a surface anisotropy field will force the magnetic moments out of the plane. This effect reduces as the films get thicker.

Then, we discuss the dependence between the Gilbert damping and the film thickness as plotted in figure 3.20a. We observe an exponential decrease in α as the film thickness increases. For the 10 nm film, we report a large damping of 0.04 and then it reduced by a factor of 2 for the 20 nm film. These values are well compared to the results of Yan et al. [29], Sharma et al. [33], and Barati et al. [34]. By plotting, α vs. $1/t$ we observe a linear dependence that can be expressed as

$$\alpha_G = 0.26 \times 10^{-9} \times \frac{1}{t} + 4 \times 10^{-3} \tag{3.5}$$

It clearly shows that surface effects play a major role in the large increase of the damping for thin films. When the thickness approached the bulk value, an extremely low value of α of magnitude 4×10^{-3} could be achieved. A similar value of 5×10^{-3} has been reported in the literature Schoen et al. [22] .

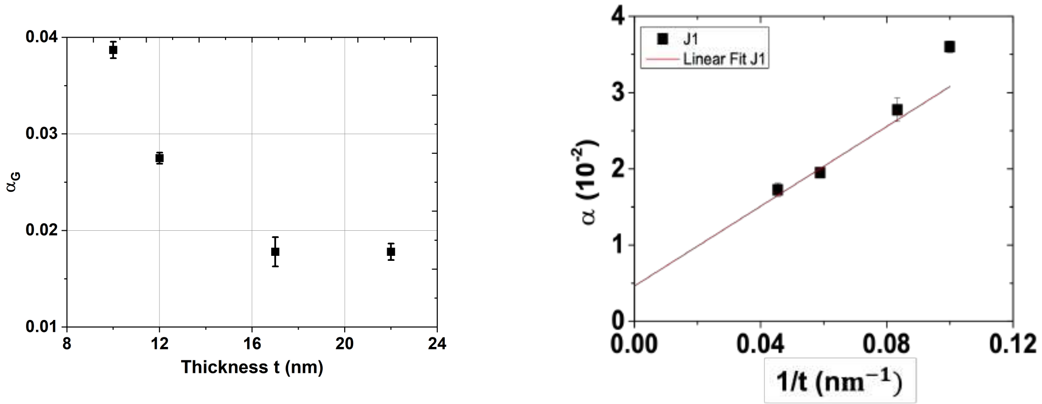

(a)

(b)

Figure 3.20: Variation of the Gilbert Damping coefficient as a function of the (a) t and (b) 1/t. Red lines represent the linear fits

3.7 Spin-Pumping in CoFe/Pt bilayers

The last aim of this thesis work is to study the spin pumping effect, a recent concept in spintronics, which is realized when a heavy metal is deposited on top of a ferromagnetic. For this purpose, we use the sputtering machine to deposit a few nanometers of Pt on top of the CoFe films forming bilayers of CoFe/Pt over the sample S16. The sample is grown using Laser energy 400 mJ at room temperature for 90 minutes with a thickness of about 18 nm. Initially, one sample was cut in half and a layer of 5nm of Pt was sputtered on top. Then, a full FMR analysis is done as discussed to determine the impact of the Pt layer on the magnetic properties. Figure compares the results of two films with and without Pt. The results are summarized in Table. 3.6. Notice that the saturation magnetization is identical for both films. However, a noticeable increase in the FWHM is observed for the CoFe/Pt bilayer. Therefore, the Gilbert damping coefficient is mainly affected when we measure an increase of 20% from 0.015 to 0.019. The contribution of the spin pumping ($\alpha_{spinpumping}$) is

$$\alpha_{spinpumping} = \alpha_{CoFe/Pt} - \alpha_{coFe}$$

which is about 0.004 for this film.

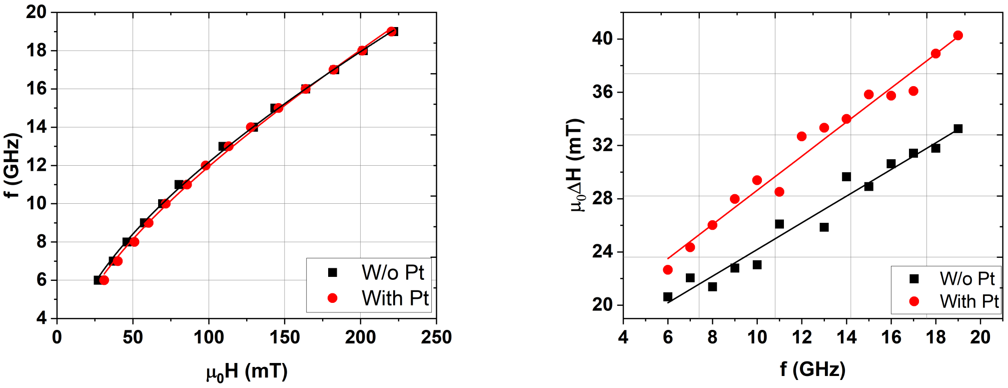

(a) Frequency-field dependence

(b) FWHM vs. frequency

Figure 3.21: BFMR Results of the samples with and w/o the sputtered Pt layer along with the corresponding fits

Sample	$\mu_0 M_S$ (T)	α_G	$\mu_0 \Delta H_0$ (T)	Spectrum
W/o Pt	1.537	0.015	0.014	A.3a
With Pt	1.566	0.019	0.016	A.3b

Table 3.6: Perspective magnetic properties of the samples with and w/o Pt

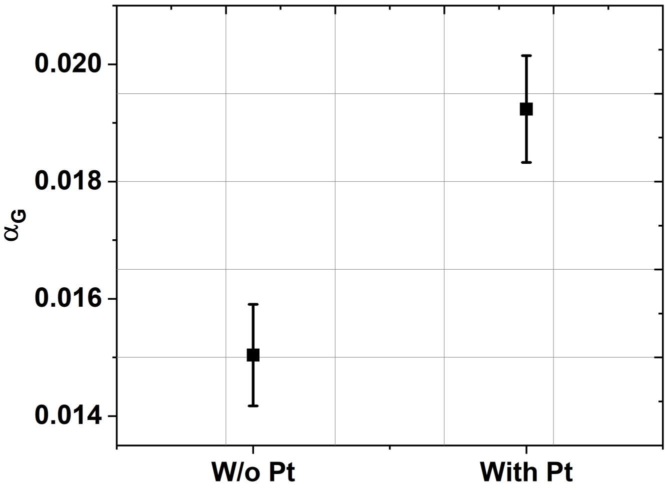

Figure 3.22: α_G of a Sample with and w/o Pt

The change in α_G is attributed to the spin pumping effect that is explained in 1.3.5.

Furthermore, we want to study the characteristics of the spin pumping mechanism relative to the thickness of the Pt layer on top of the film.

3.7.1 *S3 Series - Effect of Platinum Thickness*

The CoFe/Pt bilayers are characterized by two key parameters: (i) the efficiency of the spin transport across the CoFe-Pt interface denoted by $g^{\uparrow\downarrow}$, and (ii) the spin diffusion length λ_{Pt} in the Pt layer. We can determine these parameters by performing a series of CoFe/Pt bilayers while varying the thickness of Pt. We do this, by cutting the sample S9 into three similar pieces where 3 nm and 6 nm of Pt layers are sputtered on each piece. As discussed above, we perform the broadband-FMR measurements on these samples, where we notice no change in the saturation magnetization. On the contrary, we report an increase in the damping coefficient with the increases of Pt thickness due to the spin pumping as summarized in 3.7.

Sample	$\mu_0 M_S$ (T)	α_G	$\mu_0 \Delta H_0$ (T)	Spectrum
W/o Pt	1.544	0.0187	0.0191	A.2a
Pt - 3 nm	1.534	0.0210	0.0171	A.4a
Pt - 6 nm	1.531	0.0209	0.0199	A.4b

Table 3.7: Perspective magnetic properties of S3 Series

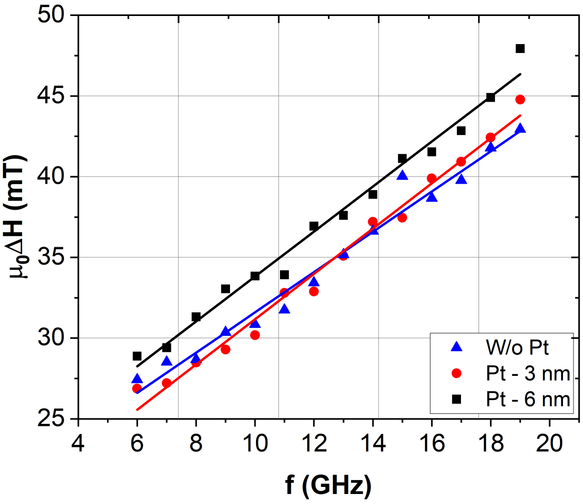

Figure 3.23: FWHM vs. frequency for three samples with different Pt thicknesses

In these films, the total damping is decomposed into two factors, the intrinsic Gilbert damping (α_0) and the spin pumping (α_{sp}) contributions written as

$$\Delta\alpha_{sp} = \alpha_{tot} - \alpha_0 \tag{3.6}$$

The spin pumping contribution can be expressed in terms of $g^{\uparrow\downarrow}$ and λ_{SD}[35]

$$\alpha_{sp} = \frac{g\mu_B g^{\uparrow\downarrow}}{4\pi M_S t_{CoFe}} \left(1 - e^{-\frac{2t_{Pt}}{\lambda_{SD}}}\right) \tag{3.7}$$

Where g is the spectroscopic factor, μ_B is the Bohr Magneton, $g^{\uparrow\downarrow}$ is the spin mixing conductance, and λ_{SD} is the spin diffusion coefficient of Pt.

Figure 3.24 shows a plot of α_{sp} vs. the Pt thickness, which shows an increase of the spin-pumping contribution to the damping and saturation at the thick Pt layer. By fitting this data to 3.7, we estimate the characteristics of CoFe/Pt bilayers $g^{\uparrow\downarrow}$ of $5.28 \times 10^{19} m^{-2}$ and λ_{SD} of $2.25 nm$. These parameters are in close agreement with other reported values in the literature by Keller et al. [35].

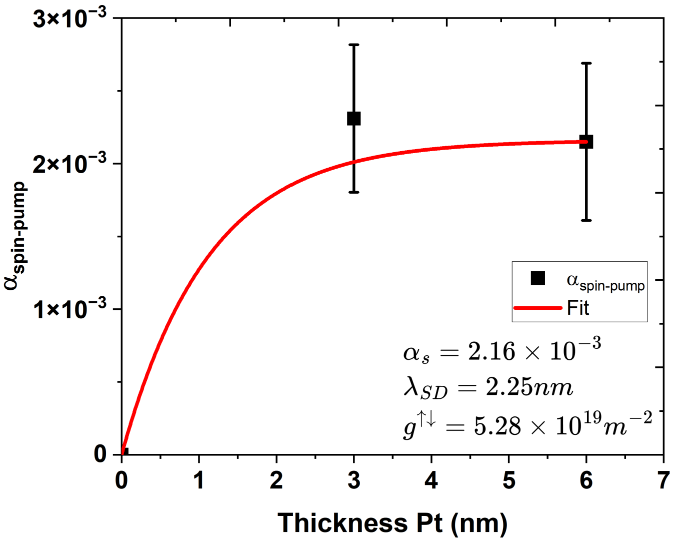

Figure 3.24: Variation of α_G as a function of Pt thickness layer t_{Pt}

Chapter 4

Conclusions and Further Studies

In conclusion, we have performed a comprehensive study on the characteristics of $Co_{60}Fe_{40}$ thin films prepared using the Pulsed Laser Deposition (PLD). A set of techniques are used to characterize these thin films such as Scanning electron microscopy, element dispersive spectroscopy, and the profilometer. The magnetic characteristics of these thin films were mainly accessed from a broadband ferromagnetic resonance measurement. The results of this work can be summarized:

1- The fabrication of thin films at different annealing temperatures revealed a maximum saturation magnetization (M_S) was achieved at $T = 373K$. This phenomenon can be attributed to phase transitions around that temperature, optimizing the summation of the magnetic moment. Furthermore, a direct relationship between temperature and the Gilbert damping parameter (α_G) was established. As annealing temperatures increased, there was a pronounced escalation in precessional damping. These findings contribute valuable insights into the effects of annealing temperatures on film properties, particularly concerning magnetic characteristics and precessional damping.

2- While increasing the laser energy, nanometer-thick films were successfully produced within the range of 10 to 22 nm. An investigation into the thickness dependence of magnetization and damping revealed a discernible pattern: thicker films exhibited higher magnetization (1.6 T) and lower damping (α of 0.017). Importantly, the findings underscored the significant contribution of surface effects to both saturation magnetization (M_S) and the damping factor (α).

3- We explored the phenomenon of spin pumping by employing the sputtering technique to deposit a 5 nm Platinum (Pt) layer on top of the CoFe layer. This bilayer configuration yielded a notable increase of 20% in the damping parameter (α). This observed increase in the damping parameter was attributed to the influence of the spin-pumping mechanism induced by the Pt layer.

4- Moreover, we explore the effect of depositing platinum (Pt) with varying thicknesses, to determine the key parameters characterizing the spin dynamics in the CoFe/Pt system. Specifically, we determined the spin mixing conductance ($g^{\uparrow\downarrow}$), revealing a value of $5.3 \times 10^{19} m^{-2}$. Additionally, we calculated the spin diffusion length of Pt, denoted as λ_{SD}, which was found to be 2.25 nm.

Appendix A

Signal Spectrum

This Appendix will mainly be used to visualize the different signals computed for each sample at different frequencies. This is done to declutter the thesis and have the reader look at the difference in signal and spectrums at ease.

Initially, the first stack of spectrums will belong to the 4 samples grown at different temperatures that were analyzed in section 3.5. Their full BFMR signal spectrum is plotted below in A.1.

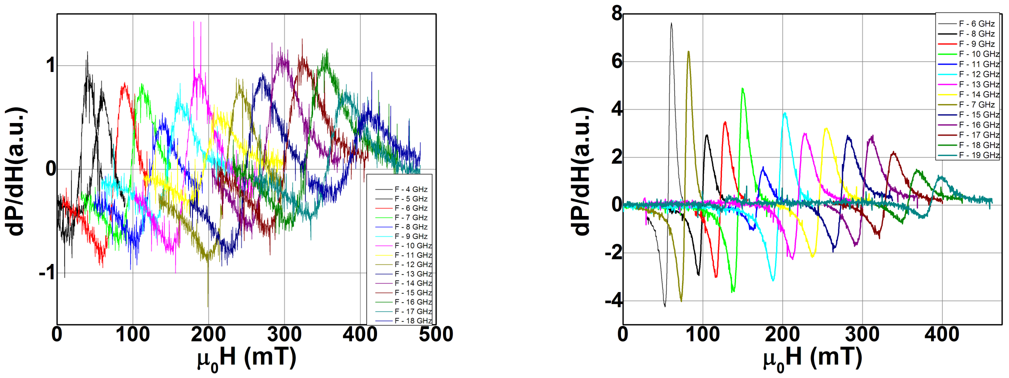

(a) The full spectrum of S6

(b) The full spectrum of S7

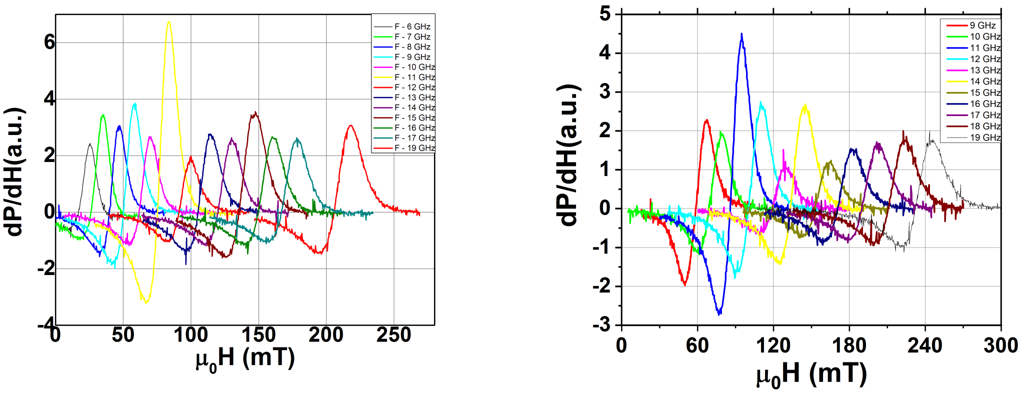

(c) The full spectrum of S9

(d) The full spectrum of S10

Figure A.1: The full spectrum of the samples that were referenced in 3.5

The second batch of spectrums will belong to the samples grown in a variation of thicknesses, analyzed in 3.6. Their perspective BFMR spectrums are illustrated below in A.2.

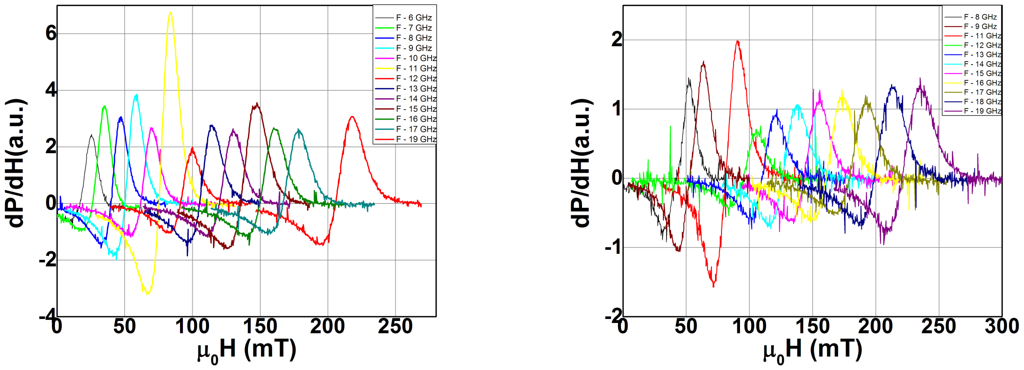

(a) The full spectrum of S9

(b) The full spectrum of S11

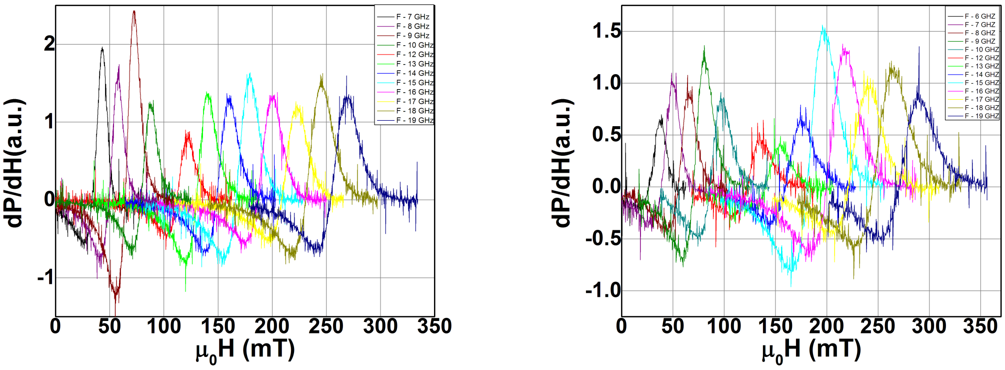

(c) The full spectrum of S12

(d) The full spectrum of S13

Figure A.2: The full spectrum of the samples that were referenced in 3.6

Regarding the two samples discussed in 3.7, the samples' perspective spectrums can be illustrated here:

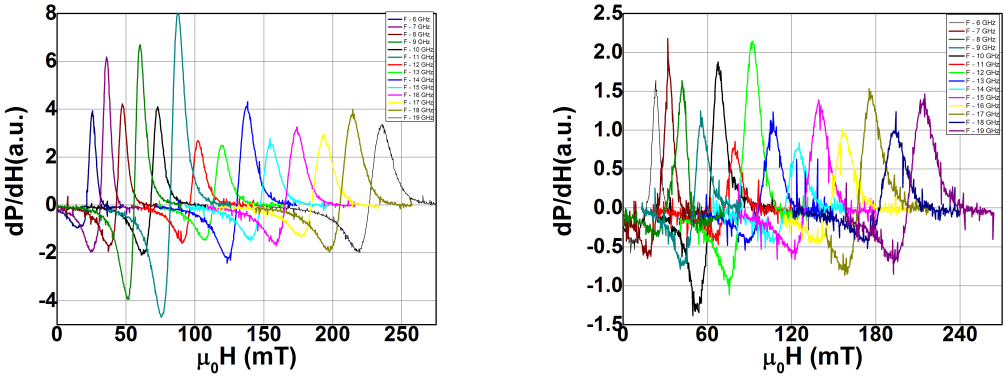

(a) Full Spectrum W/o Pt Layer

(b) Full Spectrum With the 5 nm Pt Layer

Figure A.3: The full spectrum of the samples that were referenced in 3.7

Afterward, the sample was cut into three parts and Pt layers of different thicknesses were sputtered to study the effect of Pt thickness layer on the spin-pumping contribution. Their spectrums are as follows:

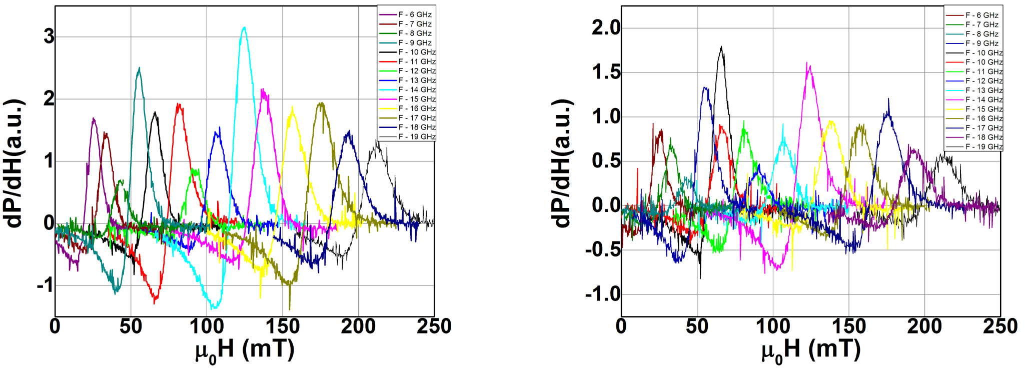

(a) Full Spectrum of 3 nm Pt Layer

(b) Full Spectrum of 6 nm Pt Layer

Figure A.4: The full spectrum of the samples that were referenced in 3.7.1

BIBLIOGRAPHY

[1] S. Blundell and D. Thouless, "*Magnetism in Condensed Matter*," en, *American Journal of Physics*, vol. 71, no. 1, pp. 94–95, Jan. 2003, ISSN: 0002-9505, 1943-2909. DOI: 10.1119/1.1522704. [Online]. Available: https://pubs.aip.org/ajp/article/71/1/94/1038735/Magnetism-in-Condensed-Matter (visited on 11/26/2023).

[2] A. A. Kaufman, R. O. Hansen, and R. L. Kleinberg, "Chapter 6 Paramagnetism, Diamagnetism, and Ferromagnetism," en, in *Methods in Geochemistry and Geophysics*, vol. 42, Elsevier, 2008, pp. 207–254, ISBN: 978-0-444-52995-4. DOI: 10.1016/S0076-6895(08)00006-1. [Online]. Available: https://linkinghub.elsevier.com/retrieve/pii/S0076689508000061 (visited on 11/15/2023).

[3] N. Magnani, "Ferromagnetism," en, in *Encyclopedia of Condensed Matter Physics*, Elsevier, 2005, pp. 201–210, ISBN: 978-0-12-369401-0. DOI: 10.1016/B0-12-369401-9/01115-3. [Online]. Available: https://linkinghub.elsevier.com/retrieve/pii/B0123694019011153 (visited on 11/25/2023).

[4] V. Iacovacci, G. Lucarini, L. Ricotti, and A. Menciassi, "Magnetic field-based technologies for lab-on-a-chip applications," in Jun. 2016, ISBN: 978-953-51-2457-3. DOI: 10.5772/62865.

[5] J. Bransky and A. Hirsch, "Magnetic anisotropy in ferromagnetic thin films," en, *Physica*, vol. 34, no. 3, pp. 349–360, Jan. 1967, ISSN: 00318914. DOI: 10.1016/0031-8914(67)90002-X. [Online]. Available: https://linkinghub.elsevier.com/retrieve/pii/003189146790002X (visited on 11/25/2023).

[6] L. Landau and E. Lifshitz, "On the theory of the dispersion of magnetic permeability in ferromagnetic bodies," en, in *Perspectives in Theoretical Physics*, Elsevier, 1992, pp. 51–65, ISBN: 978-0-08-036364-6. DOI: 10.1016/B978-0-08-036364-6.50008-9. [Online]. Available: https://linkinghub.elsevier.com/retrieve/pii/B9780080363646500089 (visited on 11/25/2023).

[7] A. Gurevich and G. Melkov, *Magnetization Oscillations and Waves*, en, 1st ed. CRC Press, Dec. 2020, ISBN: 978-0-13-874848-7. DOI: 10.1201/9780138748487. [Online]. Available: https://www.taylorfrancis.com/books/9780429611278 (visited on 11/26/2023).

[8] C. Kittel, "Ferromagnetic resonance," *J. phys. radium*, vol. 12, no. 3, pp. 291–302, 1951.

[9] L. Berger, "A simple theory of spin-wave relaxation in ferromagnetic metals," en, *Journal of Physics and Chemistry of Solids*, vol. 38, no. 12, pp. 1321–1326, Jan. 1977, ISSN: 00223697. DOI: 10.1016/0022-3697(77)90002-6. [Online]. Available: https://linkinghub.elsevier.com/retrieve/pii/0022369777900026 (visited on 12/26/2023).

[10] V. Kamberský, "On the Landau–Lifshitz relaxation in ferromagnetic metals," en, *Canadian Journal of Physics*, vol. 48, no. 24, pp. 2906–2911, Dec. 1970, ISSN: 0008-4204, 1208-6045. DOI: 10.1139/p70-361. [Online]. Available: http://www.nrcresearchpress.com/doi/10.1139/p70-361 (visited on 12/26/2023).

[11] D. Thonig and J. Henk, "Gilbert damping tensor within the breathing Fermi surface model: Anisotropy and non-locality," *New Journal of Physics*, vol. 16, no. 1, p. 013 032, Jan. 2014, ISSN: 1367-2630. DOI: 10.1088/1367-2630/16/1/013032. [Online]. Available: https://iopscience.iop.org/article/10.1088/1367-2630/16/1/013032 (visited on 12/04/2023).

[12] K. Gilmore, Y. U. Idzerda, and M. D. Stiles, "Spin orbit precession damping in transition metal ferromagnets," 2008, Publisher: arXiv Version Number: 1. DOI: 10.48550/ARXIV.0801.0549. [Online]. Available: https://arxiv.org/abs/0801.0549 (visited on 12/26/2023).

[13] S. Mankovsky, D. Ködderitzsch, G. Woltersdorf, and H. Ebert, "First-principles calculation of the Gilbert damping parameter via the linear response formalism with application to magnetic transition metals and alloys," en, *Physical Review B*, vol. 87, no. 1, p. 014 430, Jan. 2013, ISSN: 1098-0121, 1550-235X. DOI: 10.1103/PhysRevB.87.014430. [Online]. Available: https://link.aps.org/doi/10.1103/PhysRevB.87.014430 (visited on 12/29/2023).

[14] I. Turek, J. Kudrnovský, and V. Drchal, "Nonlocal torque operators in *ab initio* theory of the Gilbert damping in random ferromagnetic alloys," en, *Physical Review B*, vol. 92, no. 21, p. 214 407, Dec. 2015, ISSN: 1098-0121, 1550-235X. DOI: 10.1103/PhysRevB.92.214407. [Online]. Available: https://link.aps.org/doi/10.1103/PhysRevB.92.214407 (visited on 12/29/2023).

[15] M. Finazzi, F. Bottegoni, C. Zucchetti, *et al.*, "Optical Orientation and Inverse Spin Hall Effect as Effective Tools to Investigate Spin-Dependent Diffusion," en, *Electronics*, vol. 5, no. 4, p. 80, Nov. 2016, ISSN: 2079-9292. DOI: 10.3390/electronics5040080. [Online]. Available: http://www.mdpi.com/2079-9292/5/4/80 (visited on 11/25/2023).

[16] C. Swindells and D. Atkinson, "Interface enhanced precessional damping in spintronic multilayers: A perspective," *Journal of Applied Physics*, vol. 131, p. 170 902, May 2022. DOI: 10.1063/5.0080267.

[17] V. E. Demidov, S. Urazhdin, H. Ulrichs, *et al.*, "Magnetic nano-oscillator driven by pure spin current," vol. 3459, p. 1028, 2012. DOI: 10.1038/nmat3459.

[18] M. Haidar, A. Awad, M. Dvornik, R. Khymyn, A. Houshang, and J. Åkerman, "A single layer spin-orbit torque nano-oscillator," *Nature Communications*, vol. 10, p. 2362, 2019. DOI: 10.1038/s41467-019-10120-4.

[19] M. Haidar, M. Ranjbar, M. Balinsky, R. K. Dumas, S. Khartsev, and J. Åkerman, "Thickness- and temperature-dependent magnetodynamic properties of yttrium iron garnet thin films," vol. 117, p. 17D119, 2015.

[20] M. Haidar, B. El-Khoury, and S. Isber, "Broadband ferromagnetic resonance of ultrathin yttrium iron garnet films by pulsed laser deposition: Effects of deposition parameters," *Journal of Magnetism and Magnetic Materials*, vol. 580, p. 170 888, 2023, ISSN: 0304-8853. DOI: https://doi.org/10.1016/j.jmmm.2023.170888. [Online]. Available: https://www.sciencedirect.com/science/article/pii/S0304885323005371.

[21] M. A. W. Schoen, D. Thonig, M. L. Schneider, *et al.*, "Ultra-low magnetic damping of a metallic ferromagnet," *Nature Physics*, vol. 12, p. 839, 2016. DOI: 10.1038/nphys3770.

[22] M. A. W. Schoen, J. Lucassen, H. T. Nembach, *et al.*, "Magnetic properties in ultrathin 3 d transition-metal binary alloys. II. Experimental verification of quantitative theories of damping and spin pumping," en, *Physical Review B*, vol. 95, no. 13, p. 134 411, Apr. 2017, ISSN: 2469-9950, 2469-9969. DOI: 10.1103/PhysRevB.95.134411. [Online]. Available: http://link.aps.org/doi/10.1103/PhysRevB.95.134411 (visited on 12/04/2023).

[23] M. A. W. Schoen, J. M. Shaw, H. T. Nembach, M. Weiler, and T. J. Silva, "Radiative damping in waveguide-based ferromagnetic resonance measured via analysis of perpendicular standing spin waves in sputtered permalloy films,"

Phys. Rev. B, vol. 92, p. 184 417, 18 Nov. 2015. DOI: 10.1103/PhysRevB.92.184417. [Online]. Available: https://link.aps.org/doi/10.1103/PhysRevB.92.184417.

[24] J. M. Lock, "Eddy current damping in thin metallic ferromagnetic films," *British Journal of Applied Physics*, vol. 17, no. 12, pp. 1645–1647, Dec. 1966, ISSN: 0508-3443. DOI: 10.1088/0508-3443/17/12/415. [Online]. Available: https://iopscience.iop.org/article/10.1088/0508-3443/17/12/415 (visited on 12/05/2023).

[25] W.-J. Liu, Y.-H. Chang, C.-C. Chiang, *et al.*, "Effect of Annealing and Thickness of Co40Fe40Yb20 Thin Films on Various Physical Properties on a Glass Substrate," en, *Materials*, vol. 15, no. 23, p. 8509, Nov. 2022, ISSN: 1996-1944. DOI: 10.3390/ma15238509. [Online]. Available: https://www.mdpi.com/1996-1944/15/23/8509 (visited on 12/19/2023).

[26] R. C. Bhatt, L.-X. Ye, N. T. Hai, J.-C. Wu, and T.-h. Wu, "Spin-flop led peculiar behavior of temperature-dependent anomalous Hall effect in Hf/Gd-Fe-Co," en, *Journal of Magnetism and Magnetic Materials*, vol. 537, p. 168 196, Nov. 2021, ISSN: 03048853. DOI: 10.1016/j.jmmm.2021.168196. [Online]. Available: https://linkinghub.elsevier.com/retrieve/pii/S0304885321004728 (visited on 12/19/2023).

[27] S. G. Greculeasa, A.-E. Stanciu, A. Leca, *et al.*, "Influence of Thickness on the Magnetic and Magnetotransport Properties of Epitaxial La0.7Sr0.3MnO3 Films Deposited on STO (0 0 1)," en, *Nanomaterials*, vol. 11, no. 12, p. 3389, Dec. 2021, ISSN: 2079-4991. DOI: 10.3390/nano11123389. [Online]. Available: https://www.mdpi.com/2079-4991/11/12/3389 (visited on 12/20/2023).

[28] D. Velázquez Rodriguez, J. Gómez, G. Alejandro, *et al.*, "Relaxation mechanisms in ultra-low damping Fe80Co20 thin films," en, *Journal of Magnetism and Magnetic Materials*, vol. 504, p. 166 692, Jun. 2020, ISSN: 03048853. DOI: 10.1016/j.jmmm.2020.166692. [Online]. Available: https://linkinghub.elsevier.com/retrieve/pii/S030488532030072X (visited on 12/07/2023).

[29] H. Yan, G. J. Omar, Z. T. Zhao, L. Z. Shiuh, and A. Ariando, "High-quality NiFe thin films on oxide/non-oxide platforms via pulsed laser deposition at room temperature," 2023, Publisher: arXiv Version Number: 1. DOI: 10.48550/ARXIV.2304.00357. [Online]. Available: https://arxiv.org/abs/2304.00357 (visited on 11/16/2023).

[30] R. Ranjbar, K. Suzuki, A. Sugihara, T. Miyazaki, Y. Ando, and S. Mizukami, “Engineered Heusler Ferrimagnets with a Large Perpendicular Magnetic Anisotropy,” en, *Materials*, vol. 8, no. 9, pp. 6531–6542, Sep. 2015, ISSN: 1996-1944. DOI: 10.3390/ma8095320. [Online]. Available: http://www.mdpi.com/1996-1944/8/9/5320 (visited on 12/31/2023).

[31] M. Belmeguenai, M. S. Gabor, Y. Roussigne, F. Zighem, S. M. Cherif, and C. Tiusan, “Perpendicular Magnetic Anisotropy in Co_2 FeAl Thin Films: Effect of Annealing Temperature,” *IEEE Transactions on Magnetics*, vol. 51, no. 11, pp. 1–4, Nov. 2015, ISSN: 0018-9464, 1941-0069. DOI: 10.1109/TMAG.2015.2435815. [Online]. Available: http://ieeexplore.ieee.org/document/7111291/ (visited on 12/31/2023).

[32] V. A. Bautin, A. G. Seferyan, M. S. Nesmeyanov, and N. A. Usov, “Magnetic properties of polycrystalline cobalt nanoparticles,” en, *AIP Advances*, vol. 7, no. 4, p. 045 103, Apr. 2017, ISSN: 2158-3226. DOI: 10.1063/1.4979889. [Online]. Available: https://pubs.aip.org/adv/article/7/4/045103/22079/Magnetic-properties-of-polycrystalline-cobalt (visited on 01/07/2024).

[33] V. Sharma, R. K. Ghosh, and B. K. Kuanr, “Influence of ferromagnetic layer thickness on the Gilbert damping and magnetocrystalline anisotropy in PLD grown epitaxial Co2FeSi Heusler alloy thin films,” en, *Results in Surfaces and Interfaces*, vol. 6, p. 100 052, Feb. 2022, ISSN: 26668459. DOI: 10.1016/j.rsurfi.2022.100052. [Online]. Available: https://linkinghub.elsevier.com/retrieve/pii/S2666845922000083 (visited on 09/14/2023).

[34] E. Barati, M. Cinal, D. M. Edwards, and A. Umerski, “Calculation of Gilbert damping in ferromagnetic films,” *EPJ Web of Conferences*, vol. 40, P. Tiberto, M. Affronte, F. Casoli, *et al.*, Eds., p. 18 003, 2013, ISSN: 2100-014X. DOI: 10.1051/epjconf/20134018003. [Online]. Available: http://www.epj-conferences.org/10.1051/epjconf/20134018003 (visited on 11/26/2023).

[35] S. Keller, L. Mihalceanu, M. R. Schweizer, *et al.*, “Determination of the spin Hall angle in single-crystalline Pt films from spin pumping experiments,” *New Journal of Physics*, vol. 20, no. 5, p. 053 002, May 2018, ISSN: 1367-2630. DOI: 10.1088/1367-2630/aabc46. [Online]. Available: https://iopscience.iop.org/article/10.1088/1367-2630/aabc46 (visited on 12/18/2023).